Joint Spectrum, Precoding, and Phase Shifts Design for RIS-Aided Multiuser MIMO THz Systems

Ali Mehrabian, *Student Member, IEEE*, and Vincent W.S. Wong, *Fellow, IEEE*

***Abstract*—Terahertz (THz) wireless systems aim to support content-rich applications with ultra-high data rate. Due to high molecular absorption, THz signals experience severe path loss over long distance. To alleviate distance limitation, reconfigurable intelligent surface (RIS) can improve the coverage range. Adaptive sub-band bandwidth (ASB) allocation can mitigate absorption attenuation by allocating THz sub-bands with variable bandwidth to the users. However, in ASB allocation, since the bandwidth of sub-bands may not be known *a priori*, accurate channel estimation is challenging. To overcome this issue, in this paper, we propose a metapath-based heterogeneous graph-transformer network (MHGphormer) to bypass the channel estimation phase. We formulate a sum-rate maximization problem with quality-of-service (QoS) constraints in a RIS-aided multiuser multiple-input multiple-output (MU-MIMO) THz system to optimize the precoding, phase shifts, and ASB allocation. The proposed MHGphormer parameterizes the mapping from input (e.g., location information, users' minimum data rate) to the optimized system parameters via unsupervised learning. The proposed MHGphormer has the permutation invariance/equivariance property. It can be applied to systems with different number of users. Simulation results show that our proposed MHGphormer achieves a higher system sum-rate when compared with the homogeneous graph neural network, unsupervised deep neural network, and alternating optimization baseline algorithms.**

***Index Terms*—Heterogeneous graph neural networks, multiuser multiple-input multiple-output, reconfigurable intelligent surface, spectrum allocation, terahertz communication.**

I. Introduction

With the advancement of the sixth-generation (6G) systems, terahertz (THz) communication is envisioned as a promising solution to provide users with ultra-high throughput [2]. While the current fifth-generation (5G) systems can use millimeter-wave technology in the $30-300$ gigahertz (GHz) frequency range, the THz band spectrum range ($0.1-10$ THz) enables much higher data rate ranging from tens of gigabits to terabits per second and lower latency of the order of microseconds [3]. These advantages create a unique opportunity to advance the progress of many emerging applications, such as autonomous driving and extended reality. However, THz technology introduces previously unexplored challenges, which require novel approaches to address them.

Since the energy of higher frequency signals is more easily absorbed by the atmospheric environment, they experience more severe path loss [4]. For THz signals, in addition to the spreading loss and the higher channel sparsity, atmospheric absorption can significantly affect the propagation channel for users, which can lead to performance degradation. Specific frequencies in the THz band with the highest absorption of electromagnetic radiation are called molecular absorption coefficient peaks. They divide the THz spectrum into multiple ultra-wide THz transmission windows (TWs) [5]. The spectrum range of each TW is further divided into a set of sub-bands for allocation to the users [6]. For THz spectrum allocation with multiple sub-bands, some works proposed equal sub-band bandwidth (ESB) allocation. The authors in [5] investigated distance-dependent sub-band bandwidth allocation by considering the inter-symbol and inter-band interferences in multiple TWs. In [6], transmit power allocation and sub-band assignment for a non-orthogonal multiple access-aided THz system is studied. However, due to the frequency-selective nature of THz signals, absorption loss variations within the sub-bands are high in ESB allocation. As a result, new techniques need to be explored for THz spectrum management.

Recently, adaptive sub-band bandwidth (ASB) allocation has been proposed, in which the bandwidth allocated to each sub-band can be different. This approach can further improve the spectral efficiency and mitigate the absorption loss. In [7], [8], joint sub-band assignment, ASB allocation, and power control is investigated in multi-connectivity THz systems. The authors considered single TW in [7] and multiple TWs in [8] to solve a sum-rate maximization problem iteratively using successive convex approximation. However, the joint use of multiple-input multiple-output (MIMO) technique and ASB allocation has not been investigated in [7], [8]. MIMO enables a large number of antenna arrays to obtain a high directional gain and form narrow beams to separate different users in the spatial domain [9]. As a result, precoding design in MIMO systems would be beneficial to alleviate the high absorption attenuation over long distance in multiuser THz systems.

Another technology which has the potential to mitigate the propagation distance limitation in THz systems is the reconfigurable intelligent surface (RIS) [10]. RIS consists of passive elements with adjustable phase shifts, which reflect the signals in the desired direction and create an additional link between the base station (BS) and users. Deploying a RIS can improve the coverage of BS and mitigate the distance-dependent

Manuscript received on Sept. 22, 2023; revised on Feb. 2, 2024; accepted on Feb. 27, 2024. This work was supported in part by the Natural Sciences and Engineering Research Council of Canada and the Digital Research Alliance of Canada (alliancecan.ca). This paper has been accepted for publication in part in the *Proceedings of IEEE International Conference on Communications (ICC)*, Jun. 2024 [1]. The editor coordinating the review of this paper and approving it for publication was Cunhua Pan. *(Corresponding author: Vincent W.S. Wong)*

A. Mehrabian and V. W.S. Wong are with the Department of Electrical and Computer Engineering, The University of British Columbia, Vancouver, BC, V6T 1Z4, Canada (e-mail: {alimehrabian619, vincentw}@ece.ubc.ca).

Color versions of one or more of the figures in this paper are available online at https://ieeexplore.ieee.org.

absorption loss in THz band. Most of the existing works on RIS-aided multiuser MIMO (MU-MIMO) systems assume perfect knowledge of channel estimation at the BS. In [11], an alternating optimization (AO) technique and a majorization-minimization-based algorithm are proposed for single-user and multiuser RIS-aided MIMO systems, respectively, to optimize the precoding and phase shifts. The authors in [12] proposed a double-RIS-aided MIMO system for maximization of the minimum signal-to-interference-plus-noise ratio (SINR) of all users. In [13], imperfect knowledge of channel estimation is considered, where a two time-scale transmission scheme is proposed for RIS-aided massive MIMO systems. However, since a passive RIS has no signal processing unit for channel estimation, channel parameters need to be estimated indirectly [14]. Moreover, ASB allocation in the THz band poses a new challenge. In ASB allocation, the bandwidth within each THz sub-band is unknown in advance. This makes it challenging to determine the optimal duration and number of the pilot signals in the training sequence to capture the high variations of THz channel response for accurate channel estimation. In this paper, we aim to address the following question: *How should the BS optimize the adaptive bandwidth allocation jointly with precoding and RIS phase shifts in order to achieve a high system sum-rate without channel estimation?*

Recent works considered data-driven approaches to tackle the challenges of channel estimation. The first line of work focused on using deep learning techniques without explicit channel estimation. In [14], the authors developed a homogeneous graph neural network (GNN) with one node type, which maps the pilot signals received at the BS as input features to the optimized precoding and phase shifts in a RIS-aided multiuser multiple-input single-output (MU-MISO) system. In [15], a two-tier homogeneous GNN with uplink pilot signals as input is proposed for joint user scheduling, RIS phase shifts, and precoding design. Further to the aforementioned challenges of designing the pilots, pilot signal transmission in the THz band incurs a significant amount of system overhead due to a long training sequence transmission [16]. Since the channels in many wireless systems are largely functions of distance-dependent path loss [17], the second line of research considered using other available system information to bypass the channel estimation phase. In particular, location information is utilized as input of deep neural networks (DNNs) for wireless link scheduling [17], RIS phase shifts design [18], and user association [19]. To determine the transmit power and ASB allocation in regions where the molecular absorption coefficient is nonlinear with respect to the frequency, the authors in [20] applied an unsupervised DNN using the distances between users and BS to bypass the channel estimation. However, DNNs do not comprehensively model the interaction between network entities (e.g., BS, RIS, users) and require retraining for networks with different number of users.

Recently, heterogeneous graphs have been utilized to model complex systems in which different types of entities can interact with each other [21]. Heterogenous GNNs can improve the scalability of learning algorithms with high training performance for resource allocation problems. In [22], an MU-MISO system is modeled as a bipartite heterogeneous graph, and a GNN is proposed to solve the precoding problem with different network sizes. The authors in [23] proposed a heterogeneous GNN for power allocation, which can be applied in multi-cell multiuser networks with different number of users. However, the aforementioned works (i.e., homogeneous GNNs [14], [15] and heterogeneous GNNs [22], [23]) do not consider spectrum management. Although they showed the benefits of using GNNs, several issues have yet to be addressed. First, channel gains are used as features of graph nodes and edges in [22], [23], while THz channel estimation in ASB allocation is challenging. Second, the homogeneous GNNs in [14], [15] do not consider graph edges for modeling the network topology and feature aggregation. Moreover, simple mean and max operations are used for feature aggregation, which may not be feasible in heterogeneous networks since different types of nodes can have feature vectors with different dimensions and contents [24]. Third, the proposed GNNs in [14], [15], [22], [23] are based on the message passing framework, which is prone to the over-smoothing problem [25]. This means that increasing the number of layers can cause all node embeddings to converge to a uniform embedding and limit the model to capture deep structural information, which can lead to performance degradation.

To address the aforementioned issues, in this paper, we extend our previous work in [1] to study ASB allocation with sub-band frequency reuse in a RIS-aided MU-MIMO THz system. We formulate a joint optimization problem for sum-rate maximization subject to the quality-of-service (QoS) constraints of the users by optimizing the precoding, phase shifts, and ASB allocation. Obtaining the optimal solution of the formulated nonconvex problem with coupled optimization variables is challenging. Moreover, due to the unique features of THz channel, such as high molecular absorption and spreading loss, as well as the unknown bandwidth of THz sub-bands for ASB allocation, accurate channel estimation within each sub-band is challenging. To this end, we propose a metapath-based heterogeneous graph-transformer network (MHGphormer) learning algorithm to solve the problem by bypassing the channel estimation phase. The main contributions of this paper are as follows:

- ***Heterogeneous Graph Representation***: We model the RIS-aided MU-MIMO THz system as a heterogeneous graph by defining the BS, RIS, and users as three types of nodes. The input features of different node types include the location information and users' minimum data rate. We also model the transmission links between nodes as graph edges. The graph structure is determined based on the distance information between the nodes.
- ***MHGphormer Key Advantages***: Our proposed MHGphormer has several distinct advantages. First, it can learn a mapping function between the input and system parameters in a heterogeneous network. It considers the heterogeneous information of all entities as different types of graph nodes and models the transmission links between them as graph edges. Combining and aggregating the heterogeneous information of different node types based on the structural information can improve the learning

performance. Second, our end-to-end learning algorithm can bypass the channel estimation phase. It directly maps the input features to the optimized system parameters via unsupervised training. Third, our proposed MHGphormer satisfies the permutation invariance/equivariance property. That is, if the ordering of the users is permuted, the same set of sub-band bandwidth and RIS phase shifts can be used (i.e., permutation invariance), while the precoding matrices are permuted accordingly (i.e., permutation equivariance). Moreover, the parameter dimension of our learning algorithm is scalable. Once the network has been trained, it can be applied in systems with different number of users.

- ***Performance Evaluation***: For a RIS-aided MU-MIMO THz system with six users, simulation results show that our proposed MHGphormer can achieve a system sum-rate that is 5.15%, 8.33%, and 8.82% higher than that of homogeneous GNN learning algorithm [14], unsupervised DNN learning algorithm [20], and AO algorithm [26], respectively. Moreover, our proposed MHGphormer has faster convergence in the training phase compared to the learning-based baselines. We also show the performance gains obtained from using RIS, MIMO, and ASB for improving the sum-rate in multiuser THz systems.

The remainder of this paper is organized as follows. The system model and problem formulation for RIS-aided MU-MIMO THz systems are described in Section II. In Section III, we present our proposed MHGphormer learning algorithm. Simulation results are presented in Section IV. Conclusions are given in Section V.

Notations: In this paper, we use $\mathbb{R}$ and $\mathbb{C}$ to denote the set of real and complex numbers, respectively. We use boldface upper-case letters (e.g., $\mathbf{X}$) to denote two-dimensional matrices or multi-dimensional tensors and boldface lower-case letters (e.g., $\mathbf{x}$) to denote vectors. $\mathbf{I}_N$ represents an $N \times N$ identity matrix. $\mathbf{x}[a:b]$ denotes the elements ranging from the a-th element to the b-th element of vector $\mathbf{x}$. $(\cdot)^T$ and $(\cdot)^H$ denote the transpose and conjugate transpose of a vector or matrix, respectively. $\exp(\cdot)$ denotes the exponential function. j represents the imaginary unit satisfying $j^2 = -1$. $[\cdot]$ denotes the concatenate operation. $\text{diag}(\mathbf{x})$ returns a diagonal matrix, where the diagonal elements are the elements of vector $\mathbf{x}$. $\mathbb{E}(\cdot)$ denotes the expectation. The mod operator returns the remainder after division, and $\lfloor x \rfloor$ denotes the floor function. $\|\cdot\|$ and $\|\cdot\|_F$ denote the norm of a vector and the Frobenius norm of a matrix, respectively.

II. System Model and Problem Formulation

We consider a downlink RIS-aided MU-MIMO THz system as illustrated in Fig. 1, where the system has one BS and a RIS to serve U users. Let $\mathcal{U} = \{1, \ldots, U\}$ denote the set of users. The BS is equipped with a uniform planar array (UPA) antenna which has N_{t} elements for THz signal transmission [27]. Each user is equipped with an N_{r}-element uniform linear array (ULA) antenna. The RIS has a UPA with L passive elements. Let $\mathcal{L} = \{1, \ldots, L\}$ denote the set of passive elements of the RIS. A RIS controller is placed at the BS to control the RIS

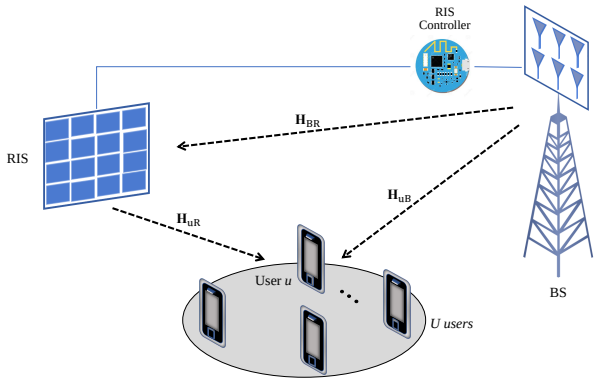

Fig. 1: Illustration of a RIS-aided MU-MIMO THz system. In addition to the direct link between BS and user $u \in \mathcal{U}$ with channel gain $\mathbf{H}_{Bu}$, RIS creates an additional link from BS-to-RIS and RIS-to-user with channel gains $\mathbf{H}_{BR}$ and $\mathbf{H}_{Ru}$, respectively.

by adjusting the phase shifts [14], [15]. For the RIS, we use $\mathbf{\Theta} = \text{diag}\left(\exp\left(j\theta_1\right), \ldots, \exp\left(j\theta_L\right)\right) \in \mathbb{C}^{L \times L}$ to denote the phase shift matrix, where $\theta_l \in \mathbb{R}$ denotes the phase shift of RIS element $l \in \mathcal{L}$. We have the following constraint for the phase shift of each RIS element:

$$\text{C1}: \quad 0 \leq \theta_l \leq 2\pi, \quad l \in \mathcal{L}. \tag{1}$$

We use $\boldsymbol{\theta} = (\theta_1, \ldots, \theta_L) \in \mathbb{R}^L$ to denote the phase shifts vector of the RIS elements.

A. THz Spectrum and Channel Model

The wide range of the THz spectrum band enables wireless systems to provide ultra-high data rate. However, a major challenge in the THz spectrum band is the high absorption attenuation, which leads to severe path loss in signal transmission [28]. As illustrated in Fig. 2(a), THz signals experience lower molecular absorption loss in THz TWs. In this paper, we consider non-overlapping ASB allocation in a TW, as shown in Fig. 2(b). Let $\mathcal{S} = \{1, 2, \ldots, S\}$ denote the set of sub-bands, where S is the total number of sub-bands. Let vectors $\mathbf{b} = (b_1, \ldots, b_S) \in \mathbb{R}^S$ and $\mathbf{f} = (f_1, f_2, \ldots, f_S) \in \mathbb{R}^S$ denote the bandwidth of the sub-bands and their central frequencies, respectively. Let b_{max} denote the maximum bandwidth of each sub-band. We have the following constraint for the bandwidth of each sub-band:

$$\text{C2}: \quad 0 \leq b_s \leq b_{\text{max}}, \quad s \in \mathcal{S}. \tag{2}$$

Let f_{start} and f_{end} denote the start and end points of the spectrum region for bandwidth allocation, respectively. We consider b_{g} as the fixed guard band bandwidth that separates the sub-bands to mitigate the inter-band interference [7]. We have:

$$f_{\text{end}} = f_{\text{start}} + \sum_{s \in \mathcal{S}} b_s + (S-1) b_{\text{g}}. \tag{3}$$

Let $b_{\text{tot}} = f_{\text{end}} - f_{\text{start}}$ denote the bandwidth of the spectrum region for allocation. We have the following constraint for the total available bandwidth:

$$\text{C3}: \quad \sum_{s \in \mathcal{S}} b_s = b_{\text{tot}} - (S-1) b_{\text{g}}. \tag{4}$$

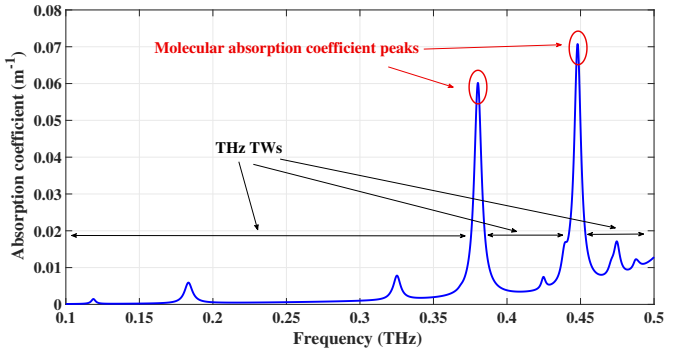

(a)

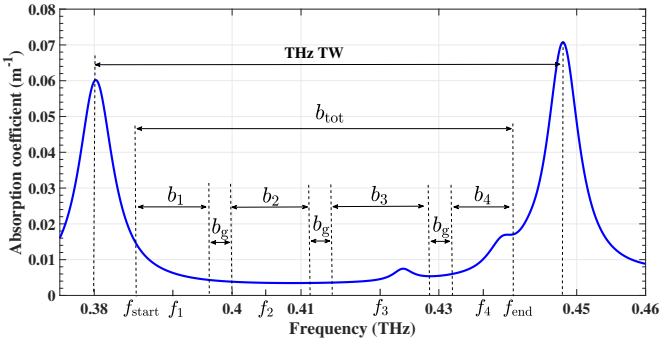

(b)

Fig. 2: Illustration of the molecular absorption coefficient $k_{\text{abs}}(f)$. (a) Molecular absorption coefficient peaks and TWs within the frequency range of $0.1 - 0.5$ THz. (b) Sub-band bandwidth allocation with total bandwidth b_{tot} and guard band b_{g} in a THz TW.

The central frequency of sub-band $s \in \mathcal{S}$ can be represented as follows:

$$f_s = \begin{cases} f_{\text{start}} + \dfrac{b_1}{2}, & s = 1, \\ f_{\text{start}} + (s-1)b_{\text{g}} + \sum_{i=1}^{s-1} b_i + \dfrac{b_s}{2}, & s \in \{2, \ldots, S\}. \end{cases} \tag{5}$$

Signal transmission in the THz band tends to be highly directional for a couple of reasons. First, there are only limited reflected components in the THz frequency range and scattered components are negligible. This means that the line-of-sight (LoS) constitutes the dominant component compared to non-line-of-sight in the THz band [3], [5], [10]. Second, to overcome the distance-dependent nature of molecular absorption loss, high-gain directional antennas are commonly used instead of omni-directional antennas with low gains [29]. This further reduces the number of available paths to a single path. Moreover, using precoding with high array gains can provide highly directional pencil beams, where each subarray generates only one beam. As a result, we consider the LoS frequency-selective fading model with the beam-squint effect for the communication channels.[1]Let d_{Bu}, d_{Ru}, and d_{BR} denote the distances between user $u \in \mathcal{U}$ and BS, user u and RIS, as well as BS and RIS, respectively. Let $\mathbf{H}_{Bu} \in \mathbb{C}^{N_{\text{r}} \times N_{\text{t}}}$, $\mathbf{H}_{Ru} \in \mathbb{C}^{N_{\text{r}} \times L}$, and $\mathbf{H}_{BR} \in \mathbb{C}^{L \times N_{\text{t}}}$ denote the BS-to-user u, RIS-to-user u, and BS-to-RIS channel gains, respectively. They can be represented as follows [31], [32]:

$$\begin{aligned} \mathbf{H}_{Bu}(d, f) = &\sqrt{G_{\text{BS}} G_u}\, \alpha\left(d_{Bu}, f\right) \exp\left(-j2\pi f \tau_{Bu}\right) \\ &\mathbf{a}_u\left(\delta_{Bu}^A, \phi_{Bu}^A\right) \mathbf{a}_B^H\left(\delta_{Bu}^D, \phi_{Bu}^D\right), \end{aligned} \tag{6a}$$

$$\begin{aligned} \mathbf{H}_{Ru}(d, f) = &\sqrt{G_u}\, \alpha(d_{Ru}, f) \exp\left(-j2\pi f \tau_{Ru}\right) \\ &\mathbf{a}_u\left(\delta_{Ru}^A, \phi_{Ru}^A\right) \mathbf{a}_R^H\left(\delta_{Ru}^D, \phi_{Ru}^D, f\right), \end{aligned} \tag{6b}$$

$$\begin{aligned} \mathbf{H}_{BR}(d, f) = &\sqrt{G_{\text{BS}}}\, \alpha\left(d_{BR}, f\right) \exp\left(-j2\pi f \tau_{BR}\right) \\ &\mathbf{a}_R\left(\delta_{BR}^A, \phi_{BR}^A, f\right) \mathbf{a}_B^H\left(\delta_{BR}^D, \phi_{BR}^D\right), \end{aligned} \tag{6c}$$

where G_u and G_{BS} denote the antenna gains for user u and BS, respectively. $\left(\delta_{Bu}^A, \phi_{Bu}^A\right)$, $\left(\delta_{Ru}^A, \phi_{Ru}^A\right)$, and $\left(\delta_{BR}^A, \phi_{BR}^A\right)$ are the azimuth and elevation angles of arrival for receiving signals in BS-to-user u, RIS-to-user u, and BS-to-RIS transmissions, respectively. Similarly, $\left(\delta_{Bu}^D, \phi_{Bu}^D\right)$, $\left(\delta_{Ru}^D, \phi_{Ru}^D\right)$, and $\left(\delta_{BR}^D, \phi_{BR}^D\right)$ denote the azimuth and elevation angles of departure for transmitted signals in BS-to-user u, RIS-to-user u, and BS-to-RIS transmissions, respectively. τ_{Bu}, τ_{Ru}, and τ_{BR} denote the delay of BS-to-user u, RIS-to-user u, and BS-to-RIS transmission paths, respectively. Moreover, $\mathbf{a}_u(\cdot) \in \mathbb{C}^{N_{\text{r}}}$, $\mathbf{a}_B(\cdot) \in \mathbb{C}^{N_{\text{t}}}$, and $\mathbf{a}_R(\cdot) \in \mathbb{C}^{L}$ denote the array steering vectors for user u, BS, and RIS, respectively. Due to the phase shift changes made by RIS elements, we consider the beam-squint effect, in which the array steering vector changes as the frequency varies. Each element of the array steering vectors for user u and BS with angles (δ, ϕ) can be calculated as follows [13], [32]:

$$\begin{aligned} \mathbf{a}_u[z] = &\frac{1}{\sqrt{N_{\text{r}}}} \exp\left(j2\pi \frac{\epsilon_{\text{user}}}{\lambda}(z-1)\cos(\delta)\sin(\phi)\right), \\ &z \in \{1, \ldots, N_{\text{r}}\}, \quad u \in \mathcal{U}, \end{aligned} \tag{7a}$$

$$\begin{aligned} \mathbf{a}_B[z] = &\frac{1}{\sqrt{N_{\text{t}}}} \exp\Bigg(j2\pi \frac{\epsilon_{\text{BS}}}{\lambda}\Bigg(\left\lfloor \frac{(z-1)}{N_x} \right\rfloor \cos(\delta)\sin(\phi) \\ &+ \text{mod}(z-1, N_y)\cos(\phi)\Bigg)\Bigg), \quad z \in \{1, \ldots, N_{\text{t}}\}, \end{aligned} \tag{7b}$$

and each element of the array steering vector for the RIS with angles (δ, ϕ) at frequency f can be calculated as follows:

$$\begin{aligned} \mathbf{a}_R[z] = &\frac{1}{\sqrt{L}} \exp\Bigg(j2\pi f \frac{\epsilon_{\text{RIS}}}{c}\Bigg(\left\lfloor \frac{(z-1)}{L_x} \right\rfloor \sin(\delta)\sin(\phi) \\ &+ \text{mod}(z-1, L_y)\cos(\phi)\Bigg)\Bigg), \quad z \in \{1, \ldots, L\}, \end{aligned} \tag{8}$$

where ϵ_{user}, ϵ_{BS}, and ϵ_{RIS} are the antenna element spacing for a user, BS, and RIS, respectively, λ is the wavelength, and c is the speed of light. Also, N_x and N_y denote the number of elements per row (i.e., horizontal direction) and number of elements per column (i.e., vertical direction) at the BS, respectively. Similarly, L_x and L_y denote the number of elements per row and per column at the RIS, respectively. The path loss factor $\alpha(d, f) \in \mathbb{R}$ with distance d between transmitter and receiver at frequency f can be calculated as

[1]In this paper, we consider the far-field channel model. In THz communication, the near-field effect can be modeled in communication channels. By considering the propagation of the spherical wavefront for the RIS and BS, the near-field effect can be modeled for users who are located in the Fresnel regions of the RIS and BS [30]. The analysis of the near-field effect is beyond the scope of this paper. Our proposed MHGphormer can be extended and applied to THz systems with consideration of the near-field effect.

follows [33]:

$$\alpha\left(d,f\right)=\underbrace{\left(\frac{c}{4\pi fd}\right)}_{\text{spreading loss}}\underbrace{\exp\left(-\frac{1}{2}k_{\text{abs}}(f)d\right)}_{\text{absorption loss}},\tag{9}$$

where $k_{\text{abs}}(f)$ is the molecular absorption coefficient which can be calculated by using the information from the HITRAN database [34], as illustrated in Fig. 2.

B. Achievable Data Rate

For the allocation of THz sub-bands to the users, a higher spectral efficiency can be obtained when users reuse the sub-bands [8], [20]. As a result, we consider sub-band frequency reuse for all users and the effect of intra-band interference. Note that the effects of inter-band interference are not considered in this paper. This is because the fixed guard bands between THz sub-bands can control inter-band interference. The achievable data rate (in bits/sec) for user $u\in\mathcal{U}$ using sub-band $s\in\mathcal{S}$ can be represented as [8]:

$$\begin{aligned}r_{u,s}=\int_{f_s-b_s/2}^{f_s+b_s/2}\log_2\Bigg(1+\gamma_{u,s}^{H}\Big(\rho_s\mathbf{I}_{N_{\text{r}}}\\+\sum_{i=1,i\neq u}^{U}\mathbf{\Gamma}_{i,s}\Big)^{-1}\gamma_{u,s}\Bigg)\,\mathrm{d}f,\end{aligned}\tag{10}$$

where ρ_s is the noise power in sub-band s and the central frequency f_s can be determined from (5). We consider the noise power as a linear function of sub-band bandwidth [8], which can be calculated by $\rho_s=b_sN_0$, where N_0 is the noise spectral density. The term $\mathbf{\Gamma}_{u,s}\in\mathbb{C}^{N_{\text{r}}\times N_{\text{r}}}$ for user u using sub-band s can be determined by $\mathbf{\Gamma}_{u,s}=\boldsymbol{\gamma}_{u,s}\boldsymbol{\gamma}_{u,s}^{H}$, where $\boldsymbol{\gamma}_{u,s}\in\mathbb{C}^{N_{\text{r}}}$ is given as:

$$\begin{aligned}\boldsymbol{\gamma}_{u,s}&=\mathbf{H}\,\mathbf{p}_{u,s}\\&=\big(\mathbf{H}_{Bu}(d_{Bu},f)\,\mathbf{p}_{u,s}\\&\quad+\mathbf{H}_{Ru}(d_{Ru},f)\,\mathbf{\Theta}\,\mathbf{H}_{BR}(d_{BR},f)\,\mathbf{p}_{u,s}\big),\end{aligned}\tag{11}$$

where $\mathbf{p}_{u,s}\in\mathbb{C}^{N_{\text{t}}}$ is the precoding vector for user $u\in\mathcal{U}$ using sub-band $s\in\mathcal{S}$. We denote $\mathbf{P}_u\in\mathbb{C}^{S\times N_{\text{t}}}$ as the precoding matrix for user u by considering all sub-bands and $\mathbf{P}=[\mathbf{P}_1,\ldots,\mathbf{P}_u,\ldots,\mathbf{P}_U]\in\mathbb{C}^{U\times S\times N_{\text{t}}}$ as the precoding tensor at the BS, respectively. We denote $\mathbf{H}\in\mathbb{C}^{N_{\text{r}}\times N_{\text{t}}}$ as the cascaded channel gain matrix. Since the rank of cascaded channel gain matrix $\mathbf{H}$ is equal to one, we consider a single data stream for signal transmission. The transmit power constraint is as follows:

$$\text{C4}:\ \sum_{u\in\mathcal{U}}\sum_{s\in\mathcal{S}}||\mathbf{p}_{u,s}||_2^2\leq P_{\max},\tag{12}$$

where $P_{\max}$ denotes the maximum transmit power of the BS. In order to guarantee that the minimum data rate requirement of user u is satisfied, we have the following per-user QoS constraint:

$$\text{C5}:\ \sum_{s\in\mathcal{S}}r_{u,s}\geq r_{u,\min},\quad u\in\mathcal{U},\tag{13}$$

where $r_{u,\min}$ corresponds to the minimum required data rate of user u.

C. Problem Formulation

In this paper, we consider sum-rate maximization to jointly optimize the precoding matrices, THz sub-bands bandwidth allocation, and phase shifts. We formulate the sum-rate maximization problem for a RIS-aided MU-MIMO THz system as follows:

$$\begin{aligned}\underset{\{\mathbf{P},\,\mathbf{b},\,\mathbf{\Theta}\}}{\text{maximize}}\quad&\sum_{u\in\mathcal{U}}\sum_{s\in\mathcal{S}}r_{u,s}\\\text{subject to}\quad&\text{constraints C1}-\text{C5}.\end{aligned}\tag{14}$$

Obtaining the optimal solution of formulated problem (14) is challenging due to the following reasons. First, the formulated problem (14) is nonconvex and the optimization variables (i.e., $\mathbf{P}$, $\mathbf{b}$, and $\mathbf{\Theta}$) are coupled. Second, calculating the objective function in (14) is difficult because the limits of the integration for determining $r_{u,s}$ in (10) depend on the optimization variable $\mathbf{b}$. Moreover, it is difficult to calculate the molecular absorption coefficient $k_{\text{abs}}(f)$ since there is no closed-form expression in terms of f for all spectrum regions in the THz band. As a result, there is no closed-form expression for the achievable data rate $r_{u,s}$ in (10) as a function of THz sub-band bandwidth $\mathbf{b}$, which makes it difficult to solve the formulated problem by using conventional optimization techniques. To address the aforementioned challenges, in the next section, we propose a learning-based MHGphormer algorithm to solve problem (14).

III. MHGphormer Learning Algorithm

In this section, we first model the RIS-aided MU-MIMO THz system as a heterogeneous graph. We then develop an unsupervised MHGphormer learning algorithm to solve problem (14).

A. Heterogeneous Graph Representation

To solve problem (14) using a learning algorithm, we consider the problem as finding an optimal mapping function $\mathcal{F}(\cdot)$, which parameterized the mapping between the input data and the precoding matrices of users (i.e., $\mathbf{P}$), sub-bands bandwidth for BS (i.e., $\mathbf{b}$) and the phase shifts at the RIS (i.e., $\mathbf{\Theta}$) while guaranteeing the constraints in problem (14) are satisfied. The mapping function $\mathcal{F}(\cdot)$ can be represented as follows:

$$\{\mathbf{P},\mathbf{b},\mathbf{\Theta}\}=\mathcal{F}\left(\mathbf{X};\mathbf{\Phi}\right),\tag{15}$$

where $\mathbf{\Phi}$ and $\mathbf{X}$ denote the set of neural network parameters and input features, respectively. Solving problem (13) is equivalent to obtaining the optimal mapping function $\mathcal{F}(\cdot)$. Utilizing the universal approximation property [35], neural networks can be trained in a data-driven manner to learn the optimal mapping function $\mathcal{F}(\cdot)$. Since the target optimization variables are coupled in problem (14), leveraging information of heterogeneous network entities (i.e., BS, RIS, and users) can improve the learning performance. Moreover, in the THz wireless systems, users may suffer from high molecular absorption attenuation and spreading loss. As a result, the transmission links between users, BS, and RIS, as well as the structural information should be modeled in a fine-grained manner to

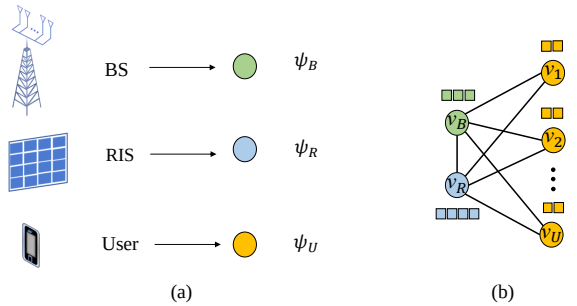

Fig. 3: An illustration of heterogeneous graph $\mathcal{G} = \{\mathcal{V}, \mathcal{E}, \Psi\}$ for the RIS-aided MU-MIMO THz system. (a) BS, RIS, and user as three types of nodes (i.e., ψ_B, ψ_R, ψ_U). (b) The graph structure of the RIS-aided MU-MIMO THz system. It consists of users, BS, and RIS as graph nodes with heterogeneous feature information and the transmission links between them as graph edges.

determine the optimized system parameters. To this end, we consider the feature information of network entities (i.e., BS, RIS, and users) as different types of graph nodes and model the transmission links between them as graph edges.

As illustrated in Fig. 3, we model the system as an undirected heterogeneous graph $\mathcal{G} = \{\mathcal{V}, \mathcal{E}, \Psi\}$. The heterogeneous graph consists of $U + 2$ nodes, where the BS and RIS are represented by nodes v_B and v_R, respectively, and the U users are represented by nodes from v_1 to v_U[2]. Let $\mathcal{V} = \{v_B, v_R, v_1, \ldots, v_U\}$ denote the set of nodes of the graph. As shown in Fig. 3(a), we denote $\Psi = \{\psi_B, \psi_R, \psi_U\}$ as the set of node types, where ψ_B, ψ_R, and ψ_U represent the BS, RIS, and user node types, respectively. Let $\mathcal{E} = \{e_{mn} \mid v_m, v_n \in \mathcal{V}\}$ denote the set of edge weights, where $e_{mn} \in \mathbb{R}$ denotes the edge weight between graph nodes v_m and $v_n \in \mathcal{V}$. We consider weighted cross-type connectivity matrices [36], [37] and model the transmission links as graph edges between the nodes in the heterogeneous graph $\mathcal{G}$. To construct the undirected weighted graph, we consider the distances between the graph nodes since the channel gain is a function of distance based on (6). Let $\mathbf{A}_{\psi_B\psi_U} \in \mathbb{R}^{1\times U}$, $\mathbf{A}_{\psi_R\psi_U} \in \mathbb{R}^{1\times U}$ and $\mathbf{A}_{\psi_B\psi_R} \in \mathbb{R}^{1\times 1}$ denote the cross-type connectivity matrices between BS and user, RIS and user, as well as BS and RIS node types, respectively. For user graph node $v_u \in \mathcal{V}$, the elements in the cross-type connectivity matrix between BS and users node types are $\mathbf{A}_{\psi_B\psi_U}[1, u] = e_{Bu} = \frac{1}{d_{Bu}}$. The elements in the cross-type connectivity matrix between RIS and user node types are $\mathbf{A}_{\psi_R\psi_U}[1, u] = e_{Ru} = \frac{1}{d_{Ru}}$. The only element in the cross-type connectivity matrix between BS and RIS node types is $\mathbf{A}_{\psi_B\psi_R}[1, 1] = e_{BR} = \frac{1}{d_{BR}}$. We further apply the softmax function to normalize the cross-type connectivity matrices as follows:

$$\hat{\mathbf{A}}_{t\psi_U}[1, u] = \text{softmax}(\mathbf{A}_{t\psi_U}[1, u]) = \frac{\exp\left(\mathbf{A}_{t\psi_U}[1, u]\right)}{\sum_{i=1}^{U} \exp\left(\mathbf{A}_{t\psi_U}[1, i]\right)}, \quad t \in \{\psi_B, \psi_R\}, \tag{16a}$$

[2]In the literature of heterogeneous GNNs, graph edges can also have different types. In this paper, we consider transmission links as the only edge type. Moreover, our proposed MHGphormer can be extended to handle scenarios with multiple BSs and RISs. The transmission links between different node types are modeled as graph edges. Other network technologies such as unmanned aerial vehicles (UAVs) and satellites can be modeled as different node types with heterogeneous feature information.

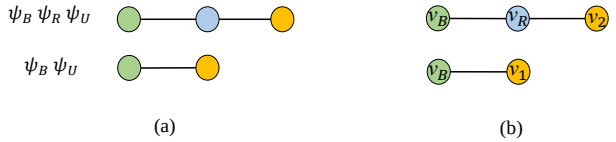

Fig. 4: An illustration of metapaths and metapath instances in heterogeneous graph $\mathcal{G} = \{\mathcal{V}, \mathcal{E}, \Psi\}$. (a) Two metapaths of the heterogeneous graph (i.e., $\psi_B\psi_R\psi_U$ and $\psi_B\psi_U$). (b) Examples of metapath instances $v_Bv_Rv_2$, v_Bv_1 for metapaths $\psi_B\psi_R\psi_U$ and $\psi_B\psi_U$, respectively.

$$\hat{\mathbf{A}}_{\psi_B\psi_R} = \text{softmax}(\mathbf{A}_{BR}) = 1. \tag{16b}$$

We denote the set of cross-type connectivity matrices as $\mathcal{A} = \{\hat{\mathbf{A}}_{\psi_B\psi_U}, \hat{\mathbf{A}}_{\psi_R\psi_U}, \hat{\mathbf{A}}_{\psi_B\psi_R}\} = \{\hat{\mathbf{A}}_{\psi_m\psi_n} \mid \psi_m, \psi_n \in \Psi\}$. Moreover, each node type of the heterogeneous graph has a feature matrix. We use the geographical location information of graph nodes and the users' minimum data rate to construct the feature matrices. To define the locations of graph nodes, we consider a three-dimensional (3-D) Cartesian coordinate system. Let $\mathbf{g}_u$, $\mathbf{g}_B$, and $\mathbf{g}_R \in \mathbb{R}^3$ denote the geographical locations of user $u \in \mathcal{U}$, BS, and RIS, respectively. The location information of users can be obtained by the proposed method in [38], where a simultaneous localization and mapping (SLAM) framework is proposed in RIS-aided systems to estimate the location of mobile users without the intervention of BS. Let $\mathbf{X}_{\psi_U} \in \mathbb{R}^{U\times 4}$, $\mathbf{X}_{\psi_B} \in \mathbb{R}^{1\times 3}$, and $\mathbf{X}_{\psi_R} \in \mathbb{R}^{1\times 3}$ denote the feature matrices of user, BS, and RIS node types, respectively. For each user node $v_u \in \mathcal{V}$, as well as BS and RIS nodes $v_B, v_R \in \mathcal{V}$, we define the feature matrices as follows:

$$\mathbf{X}_{\psi_U}[u, :] = \left[\mathbf{g}_u^T, r_{u,\min}\right], \tag{17a}$$

$$\mathbf{X}_{\psi_B}[1, :] = [\mathbf{g}_B^T], \tag{17b}$$

$$\mathbf{X}_{\psi_R}[1, :] = [\mathbf{g}_R^T]. \tag{17c}$$

We denote $\mathcal{X} = \{\mathbf{X}_{\psi_B}, \mathbf{X}_{\psi_R}, \mathbf{X}_{\psi_U}\} = \{\mathbf{X}_{\psi_m} \mid \psi_m \in \Psi\}$ as the set of feature matrices for each node type. Based on the cross-type connectivity matrices and feature matrices, the proposed MHGphormer updates the features of the nodes using all the information of different node types and graph structural information. After the update, the obtained embeddings have sufficient information to determine the optimal system parameters by learning the mapping function $\mathcal{F}(\cdot)$.

B. Metapath-based Neighbour Feature Aggregation

In heterogeneous graphs with multiple node types, the concept of metapath provides a powerful tool to capture the information between different node types based on the graph structural information [24], [39], [40]. A metapath in heterogeneous graphs is defined as a path in the form of $\mathcal{P} = \psi_m\psi_l \ldots \psi_n$ with ψ_m and $\psi_n \in \Psi$ being the source and destination node types, respectively. We denote a metapath instance $p_{mn}^{\mathcal{P}} = v_m \ldots v_n$ as a sequence of nodes following the metapath $\mathcal{P}$. Given node $v_m \in \mathcal{V}$ and the metapath $\mathcal{P}$ in graph $\mathcal{G}$, the set of metapath-based neighbours $N_m^{\mathcal{P}} = \{v_n \mid p_{mn}^{\mathcal{P}}\}$ is defined as the set of nodes which connect with node v_m via instances of metapath $\mathcal{P}$. The metapath-based neighbours at different hops create the neighbourhood of node v_m. Also, the 0-hop metapath-based neighbour of node v_m is the node itself. As an example in Fig. 4(a), consider metapaths $\psi_B\psi_R\psi_U$ and

$\psi_B\psi_U$ in graph $\mathcal{G}$. As shown in Fig. 4(b), user $v_2 \in \mathcal{V}$ is a 2-hop metapath-based neighbour of BS node $v_B \in \mathcal{V}$ via the metapath instance $p_{B2} = v_B v_R v_2$. In addition, user node $v_1 \in \mathcal{V}$ is connected to BS node $v_B \in \mathcal{V}$ via metapath instance $p_{B1} = v_B v_1$ as a one-hop metapath-based neighbour.

Since a heterogeneous graph has multiple node types, nodes can have feature information vectors with different dimensions and different contents (e.g., location information, users' minimum data rate). As a result, homogeneous GNNs with one node type cannot be directly applied to heterogeneous graphs [24]. To address this issue, we propose an MNFA module to utilize all heterogeneous feature information from different node types. Since the number of metapath instances increases exponentially with the length of a metapath [39], we propose an efficient feature aggregation module, which can be used in networks with a large number of users. The proposed MNFA module aggregates the neighbourhood feature information only once in the pre-training step. This leads to a significant reduction in computational complexity compared to repeated neighbour aggregation in each training epoch. Note that the number of hops for aggregating the neighbourhood information is fixed as a hyperparameter and can be determined based on the graph structure. In this paper, since the heterogeneous graph of the system model has three node types, we have 0-hop, 1-hop, and 2-hop metapath-based neighbours. For instance, for the user node type, the 0-hop metapath-based neighbour is the node itself (i.e., ψ_U). For the 1-hop metapath-based neighbours, we have the metapaths from user to the BS and user to the RIS (i.e., $\psi_U\psi_B$ and $\psi_U\psi_R$), respectively. Finally, the metapath sequence user-BS-RIS and the metapath sequence user-RIS-BS correspond to the 2-hop metapath-based neighbours (i.e., $\psi_U\psi_B\psi_R$ and $\psi_U\psi_R\psi_B$), respectively. We consider the following sets of metapaths for the neighborhood of user, BS, and RIS node types, respectively:

$$\mathcal{P}_U = \{\psi_U, \psi_U\psi_B, \psi_U\psi_R, \psi_U\psi_B\psi_R, \psi_U\psi_R\psi_B\}, \quad (18a)$$

$$\mathcal{P}_B = \{\psi_B, \psi_B\psi_U, \psi_B\psi_R, \psi_B\psi_R\psi_U, \psi_B\psi_U\psi_R\}, \quad (18b)$$

$$\mathcal{P}_R = \{\psi_R, \psi_R\psi_U, \psi_R\psi_B, \psi_R\psi_U\psi_B, \psi_R\psi_B\psi_U\}. \quad (18c)$$

Motivated by [39], [41], our proposed MNFA module uses the multiplication of cross-type connectivity matrices to determine the aggregated feature information for the metapath instances. This weighted-mean aggregation module takes into account the structural information between different node types in heterogeneous graphs. Given metapath $\mathcal{P} = \psi_m\psi_l\psi_k \dots \psi_n\psi_r$ and feature matrix $\mathbf{X}_{\psi_r} \in \mathcal{X}$, we perform feature aggregation for node type $\psi_m \in \Psi$ as follows:

$$\mathbf{X}^{\mathcal{P}}_{\psi_m} = \hat{\mathbf{A}}_{\psi_m\psi_l}\hat{\mathbf{A}}_{\psi_l\psi_k} \dots \hat{\mathbf{A}}_{\psi_n\psi_r}\mathbf{X}_{\psi_r}, \quad (19)$$

where $\mathbf{X}^{\mathcal{P}}_{\psi_m}$ denotes the aggregated feature matrix of node type $\psi_m \in \Psi$ for metapath $\mathcal{P}$. In Fig. 5, the feature aggregation of the user node type for different sets of metapath-based neighbours is shown as an example. Note that the aggregated results for shorter metapaths can be used as an intermediate step for longer metapaths. As an example, for the metapaths $\mathcal{P}_1 = \psi_n\psi_r$ and $\mathcal{P}_2 = \psi_m\psi_n\psi_r$, we first determine $\mathbf{X}^{\mathcal{P}_1}_{\psi_n}$ and then determine $\mathbf{X}^{\mathcal{P}_2}_{\psi_m} = \hat{\mathbf{A}}_{\psi_m\psi_n}\mathbf{X}^{\mathcal{P}_1}_{\psi_n}$. Based on (19), all the aggregated feature matrices of different node types can be calculated by considering the pre-defined metapaths in (18). For instance, for the user node type, we have $\mathbf{X}^{\psi_U}_{\psi_U} \in \mathbb{R}^{U\times 4}$, $\mathbf{X}^{\psi_U\psi_B}_{\psi_U} \in \mathbb{R}^{U\times 3}$, $\mathbf{X}^{\psi_U\psi_R}_{\psi_U} \in \mathbb{R}^{U\times 3}$, $\mathbf{X}^{\psi_U\psi_B\psi_R}_{\psi_U} \in \mathbb{R}^{U\times 3}$, and $\mathbf{X}^{\psi_U\psi_R\psi_B}_{\psi_U} \in \mathbb{R}^{U\times 3}$ as the output of the MNFA module. After performing feature aggregation in the pre-training step, we encode the aggregated features for each node type into the following representation:

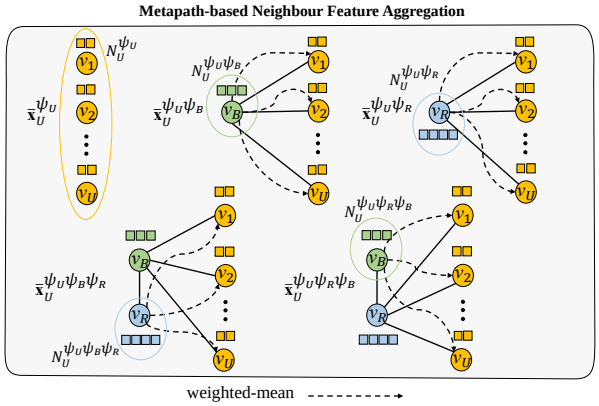

Fig. 5: An Illustration of the MNFA module for user node type. $\mathbf{X}^{\psi_U}_{\psi_U}$, $\mathbf{X}^{\psi_U\psi_B}_{\psi_U}$, $\mathbf{X}^{\psi_U\psi_R}_{\psi_U}$, $\mathbf{X}^{\psi_U\psi_B\psi_R}_{\psi_U}$, and $\mathbf{X}^{\psi_U\psi_R\psi_B}_{\psi_U}$ are the aggregated features of $N^{\psi_U}_U$, $N^{\psi_U\psi_B}_U$, $N^{\psi_U\psi_R}_U$, $N^{\psi_U\psi_B\psi_R}_U$, and $N^{\psi_U\psi_R\psi_B}_U$ as sets of metapath-based neighbours, respectively.

$$\mathbf{X}^{\mathcal{P}_U}_{\psi_U} = \left[\mathbf{X}^{\psi_U}_{\psi_U}, \mathbf{X}^{\psi_U\psi_B}_{\psi_U}, \mathbf{X}^{\psi_U\psi_R}_{\psi_U}, \mathbf{X}^{\psi_U\psi_B\psi_R}_{\psi_U}, \mathbf{X}^{\psi_U\psi_R\psi_B}_{\psi_U}\right], \quad (20a)$$

$$\mathbf{X}^{\mathcal{P}_B}_{\psi_B} = \left[\mathbf{X}^{\psi_B}_{\psi_B}, \mathbf{X}^{\psi_B\psi_U}_{\psi_B}, \mathbf{X}^{\psi_B\psi_R}_{\psi_B}, \mathbf{X}^{\psi_B\psi_R\psi_U}_{\psi_B}, \mathbf{X}^{\psi_B\psi_U\psi_R}_{\psi_B}\right], \quad (20b)$$

$$\mathbf{X}^{\mathcal{P}_R}_{\psi_R} = \left[\mathbf{X}^{\psi_R}_{\psi_R}, \mathbf{X}^{\psi_R\psi_U}_{\psi_R}, \mathbf{X}^{\psi_R\psi_B}_{\psi_R}, \mathbf{X}^{\psi_R\psi_U\psi_B}_{\psi_R}, \mathbf{X}^{\psi_R\psi_B\psi_U}_{\psi_R}\right], \quad (20c)$$

where $\mathbf{X}^{\mathcal{P}_U}_{\psi_U} \in \mathbb{R}^{U\times 16}$, $\mathbf{X}^{\mathcal{P}_B}_{\psi_B} \in \mathbb{R}^{1\times 17}$, and $\mathbf{X}^{\mathcal{P}_R}_{\psi_R} \in \mathbb{R}^{1\times 17}$ correspond to the aggregated feature matrices after encoding for user, BS and RIS node types, respectively. Finally, for each user node $v_u \in \mathcal{V}$, as well as BS and RIS nodes $v_B, v_R \in \mathcal{V}$, we define the aggregated feature vectors as $\mathbf{x}^{agg}_{u,\psi_U} = \left(\mathbf{X}^{\mathcal{P}_U}_{\psi_U}[u,:]\right)^T$, $\mathbf{x}^{agg}_{B,\psi_B} = \left(\mathbf{X}^{\mathcal{P}_B}_{\psi_B}[1,:]\right)^T$, and $\mathbf{x}^{agg}_{R,\psi_R} = \left(\mathbf{X}^{\mathcal{P}_R}_{\psi_R}[1,:]\right)^T$, respectively. Note that different graph nodes have aggregated feature vectors with different dimensions. This issue will be resolved in the next subsection. The aggregated feature vectors are used as input of the mapping function $\mathcal{F}(\cdot)$ in (15) to train the MHGphormer. Our proposed MNFA module has two distinct advantages. First, it is performed offline in the pre-training step, which allows the generalization of the proposed MHGphormer to large-scale graphs. Second, we encode the features of different neighbours at different hops into one representation for each node. This can help infer the mutual relationships between different metapath-based neighbours at different hops, which is ignored in typical GNNs based on the message passing framework.

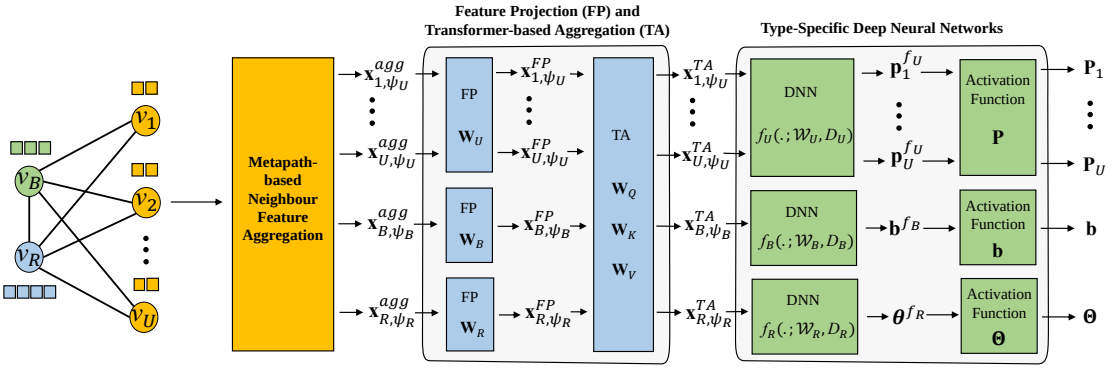

Fig. 6: The overall architecture of the proposed MHGphormer for heterogeneous graph $\mathcal{G}(\mathcal{V}, \mathcal{E}, \Psi)$ as input and system parameters $\{\mathbf{P}, \mathbf{b}, \mathbf{\Theta}\}$ as output.

C. Feature Projection and Transformer-based Aggregation

Different node types in a heterogeneous graph may have different dimensions of feature vectors. Moreover, their feature vectors may lie in different feature spaces even with the same dimension [40]. For instance, the location information of graph nodes and the data rates of user nodes are incorporated as input features, while these features cannot be directly combined together. As a result, we need to project different types of node features into the same latent space. We apply a type-specific linear transformation for each node type to project the feature information into the same latent space. For each user node $v_u \in \mathcal{V}$ with feature vector $\mathbf{x}_{u,\psi_U}^{agg}$, we have:

$$\mathbf{x}_{u,\psi_U}^{FP} = \mathbf{W}_U \mathbf{x}_{u,\psi_U}^{agg} + \mathbf{o}_U, \quad v_u \in \mathcal{V}, \tag{21}$$

where $\mathbf{W}_U \in \mathbb{R}^{Z_{FP} \times 16}$ and $\mathbf{o}_U \in \mathbb{R}^{Z_{FP}}$ are the learnable projection weights for the user node type, and Z_{FP} is a constant dimension. All users share the same projection weights $\mathbf{W}_U$ and $\mathbf{o}_U$. Similarly, for BS $v_B \in \mathcal{V}$ and RIS $v_R \in \mathcal{V}$ nodes, we have:

$$\mathbf{x}_{B,\psi_B}^{FP} = \mathbf{W}_B \mathbf{x}_{B,\psi_B}^{agg} + \mathbf{o}_B, \quad \mathbf{x}_{R,\psi_R}^{FP} = \mathbf{W}_R \mathbf{x}_{R,\psi_R}^{agg} + \mathbf{o}_R, \tag{22}$$

where $\mathbf{W}_B \in \mathbb{R}^{Z_{FP} \times 17}$, $\mathbf{o}_B \in \mathbb{R}^{Z_{FP}}$, $\mathbf{W}_R \in \mathbb{R}^{Z_{FP} \times 17}$, and $\mathbf{o}_R \in \mathbb{R}^{Z_{FP}}$ denote the learnable projection weights for BS and RIS node types, respectively. This feature projection module addresses the heterogeneity of a graph, which is due to heterogeneous feature information of different node types. After this step, the projected feature vectors of all nodes share the same dimension. We denote the set of all parameters for the feature projection module as $\mathbf{\Phi}_{FP} = \{\mathbf{W}_U, \mathbf{o}_U, \mathbf{W}_B, \mathbf{o}_B, \mathbf{W}_R, \mathbf{o}_R\}$.

To capture the mutual information of different node types and metapaths, we leverage the self-attention mechanism [42]. In heterogeneous graphs, different nodes have different impacts on the feature information of other nodes. As a result, by using the self-attention mechanism, we assign different weights to different projected feature vectors. We first concatenate the projected feature vectors as matrix $\mathbf{X}^{FP} = \left[\mathbf{x}_{1,\psi_U}^{FP}, \ldots, \mathbf{x}_{U,\psi_U}^{FP}, \mathbf{x}_{B,\psi_B}^{FP}, \mathbf{x}_{R,\psi_R}^{FP}\right]^T \in \mathbb{R}^{(U+2) \times Z_{FP}}$. Then, we map the the projected feature vector $\mathbf{x}_m^{FP} = \left(\mathbf{X}^{FP}[m,:]\right)^T$ of each node $v_m \in \mathcal{V}$ into a query vector $\mathbf{q}_m \in \mathbb{R}^{Z_{TA}}$, a key vector $\mathbf{k}_m \in \mathbb{R}^{Z_{TA}}$, and a value vector $\mathbf{v}_m \in \mathbb{R}^{Z_{FP}}$, where Z_{TA} is a constant dimension. The mutual attention weight between nodes v_m and $v_n \in \mathcal{V}$ is denoted by α_{mn}. For node v_m, the final embedding vector $\mathbf{x}_m^{TA} \in \mathbb{R}^{Z_{FP}}$ is the weighted sum of values of all the nodes plus a residual connection. The residual connection can help mitigate the gradient vanishing problem [39]. We have:

$$\mathbf{q}_m = \mathbf{W}_Q \mathbf{x}_m^{FP}, \ \mathbf{k}_m = \mathbf{W}_K \mathbf{x}_m^{FP}, \ \mathbf{v}_m = \mathbf{W}_V \mathbf{x}_m^{FP}, \tag{23a}$$

$$\alpha_{mn} = \frac{\exp\left(\mathbf{q}_m^T \mathbf{k}_n\right)}{\sum_{v_t \in \mathcal{V}} \exp\left(\mathbf{q}_m^T \mathbf{k}_t\right)}, \quad v_m, v_n \in \mathcal{V}, \tag{23b}$$

$$\mathbf{x}_m^{TA} = \beta \sum_{v_n \in \mathcal{V}} \alpha_{mn} \mathbf{v}_n + \mathbf{x}_m^{FP}, \quad v_m \in \mathcal{V}, \tag{23c}$$

where $\mathbf{W}_Q, \mathbf{W}_K \in \mathbb{R}^{Z_{TA} \times Z_{FP}}$, $\mathbf{W}_V \in \mathbb{R}^{Z_{FP} \times Z_{FP}}$, and $\beta \in \mathbb{R}$ are the learnable parameters. We denote the set of parameters for the transformer-based aggregation module as $\mathbf{\Phi}_{TA} = \{\mathbf{W}_Q, \mathbf{W}_K, \mathbf{W}_V, \beta\}$, which is shared for all the nodes. Based on the obtained values, for each user node $v_u \in \mathcal{V}$, as well as BS and RIS nodes $v_B, v_R \in \mathcal{V}$, we construct embedding vectors $\mathbf{x}_{u,\psi_U}^{TA} = \mathbf{x}_u^{TA}$, $\mathbf{x}_{B,\psi_B}^{TA} = \mathbf{x}_{U+1}^{TA}$, and $\mathbf{x}_{R,\psi_R}^{TA} = \mathbf{x}_{U+2}^{TA}$, respectively. To obtain the target system parameters, the embeddings are used as input for the type-specific DNNs.

D. Type-Specific Neural Network Design

Since the obtained embedding vectors have sufficient information from all other graph nodes, in the final step, we propose three type-specific DNNs to determine the optimized system parameters for each node type while guaranteeing the constraints in problem (14). As illustrated in Fig. 6, the neural networks $f_U(\cdot; \mathcal{W}_U, D_U)$, $f_B(\cdot; \mathcal{W}_B, D_B)$, and $f_R(\cdot; \mathcal{W}_R, D_R)$ are responsible for determining the precoding, sub-band bandwidth, and phase shifts for user, BS, and RIS node types, respectively. The last and the second last arguments of the neural networks denote the number of layers and the set of parameters for each neural network, respectively. For neural networks $f_B(\cdot; \mathcal{W}_B, D_B)$ and $f_R(\cdot; \mathcal{W}_R, D_R)$, a normalization layer, and an activation function are adopted sequentially between two adjacent linear layers. We use the rectified linear unit $\text{ReLU}(x) = \max(0, x)$ as the activation function, which is computationally efficient during the back-propagation process.

For the optimal precoding matrices, since existing software packages can manage complex-valued operations using Wirtinger calculus [43], all the learnable parameters in set $\mathcal{W}_U$ are initialized as complex values. This reduces the number of multiplication operations and computational complexity by using complex-valued arithmetic in the polar representation. We first feed the embedding vector $\mathbf{x}_{u,\psi_U}^{TA}$ of user node $v_u \in \mathcal{V}$ to the network with output vector $\mathbf{p}_u^{f_U} = f_U\left(\mathbf{x}_{u,\psi_U}^{TA}; \mathcal{W}_U, D_U\right) \in \mathbb{C}^{SN_\mathrm{t}}$. To satisfy the transmit power constraint C4, the output matrix $\mathbf{P}^{f_U} = \left[\mathbf{p}_1^{f_U}, \ldots, \mathbf{p}_U^{f_U}\right]^T \in \mathbb{C}^{U \times SN_\mathrm{t}}$ is fed through an activation function as follows:

$$\hat{\mathbf{P}} = \sqrt{P_{\max}} \frac{\mathbf{P}^{f_U}}{\|\mathbf{P}^{f_U}\|_F}. \tag{24}$$

Then, based on the normalized values $\hat{\mathbf{p}}_u = (\hat{\mathbf{P}}[u,:])^T$ for each user node $v_u \in \mathcal{V}$ and the definition for the precoding matrix in (11), we reshape the normalized values into a matrix to construct the precoding matrix for each user as follows:

$$\begin{aligned}\mathbf{P}_u = \big[&\hat{\mathbf{p}}_u[1:S],\ \hat{\mathbf{p}}_u[S+1:2S],\ \ldots,\\ &\hat{\mathbf{p}}_u[S(N_\mathrm{t}-1)+1:SN_\mathrm{t}]\big],\ \ u \in \mathcal{U}.\end{aligned} \tag{25}$$

Note that all users share the same network $f_U(\cdot; \mathcal{W}_U, D_U)$ to determine the final precoding matrices. This reduces the computational complexity in the feed-forward networks as well as the number of required training parameters [44].

For the optimal sub-band bandwidth allocation, the embedding vector $\mathbf{x}_{B,\psi_B}^{TA}$ of BS node $v_B \in \mathcal{V}$ is fed to the network with output vector $\mathbf{b}^{f_B} = f_B\left(\mathbf{x}_{B,\psi_B}^{TA}; \mathcal{W}_B, D_B\right) \in \mathbb{R}^S$. Next, to guarantee constraints C2 and C3, we first normalize each element of the output vector $\mathbf{b}^{f_B}$ as follows:

$$\hat{\mathbf{b}}[s] = \frac{\sigma\left(\mathbf{b}^{f_B}[s]\right)\left(b_\mathrm{tot} - (S-1)b_\mathrm{g}\right)}{\sum_{s' \in \mathcal{S}} \sigma\left(\mathbf{b}^{f_B}[s']\right)},\ \ s \in \mathcal{S}, \tag{26}$$

where $\sigma(x) = \dfrac{1}{\exp(-x)+1}$ denotes the element-wise sigmoid activation function mapping the output onto the range $[0,1]$. Finally, to determine the sub-band bandwidth vector $\mathbf{b}$, we feed the normalized vector $\hat{\mathbf{b}}$ to the following activation function:

$$\mathbf{b}[s] = b_{\max} - \mathrm{ReLU}\left(b_{\max} - \hat{\mathbf{b}}[s]\right),\ \ s \in \mathcal{S}, \tag{27}$$

which ensures that each element is less than or equal to $b_{\max}$. During the learning procedure, by using (26) and (27), constraint C2 is satisfied. The learning algorithm is trained in a way in order to fully utilize the available bandwidth to guarantee constraint C3.

For the optimal phase shifts, the embedding vector $\mathbf{x}_{R,\psi_R}^{TA}$ of RIS node $v_R \in \mathcal{V}$ is fed to the network with output vector $\boldsymbol{\theta}^{f_R} = f_R\left(\mathbf{x}_{R,\psi_R}^{TA}; \mathcal{W}_R, D_R\right) \in \mathbb{R}^L$. Then, we consider the obtained values as an input to the following activation function in order to satisfy the phase shift constraint C1:

$$\hat{\boldsymbol{\theta}}[l] = 2\pi\sigma(\boldsymbol{\theta}^{f_R}[l]),\ \ l \in \mathcal{L}, \tag{28}$$

which maps the values onto the range of $[0, 2\pi]$. Finally, the phase shift matrix is obtained as follows:

$$\boldsymbol{\Theta} = \mathrm{diag}\left(\exp\left(j\hat{\boldsymbol{\theta}}[1]\right), \ldots, \exp\left(j\hat{\boldsymbol{\theta}}[L]\right)\right). \tag{29}$$

We denote the set of parameters in the type-specific neural network design step as $\boldsymbol{\Phi}_{DNN} = \{\mathcal{W}_U, \mathcal{W}_B, \mathcal{W}_R\}$.

Remark 1: Our proposed MHGphormer satisfies the permutation invariance/equivariance property. That is, if the ordering of users is permuted, the same set of RIS phase shifts and sub-band bandwidth can be used (i.e., permutation invariance), while the set of precoding matrices is permuted in the same manner (i.e., permutation equivariance). This is difficult to be obtained by conventional fully connected networks, while heterogeneous GNNs can satisfy one of these properties [23]. In MHGphormer, satisfying these properties only depends on the structure of the transformer-based aggregation module, since other modules (e.g., feature projection, feed-forward networks, and normalization layers) are applied in a node-independent manner for each node type. The proposed self-attention mechanism in (23) satisfies the permutation equivariance property. For the permutation invariance property, the residual connection is removed and the query vector in (23) can be replaced by a learnable weight for each node (e.g., $\mathbf{q}_m = \mathbf{w}_m \in \mathbb{R}^{Z_{TA}},\ v_m \in \mathcal{V}$). The proof that our proposed MHGphormer satisfies the aforementioned properties can be found in the Appendix.

Remark 2: In our proposed MHGphormer, all type-specific nodes share the same modules for updating their features during the learning procedure. This means that the parameter dimension of the proposed MHGphormer does not depend on the number of nodes in each specific node type. In particular, all the user nodes share the same weights for feature projection (i.e., $\mathbf{W}_U, \mathbf{o}_U$) and transformer-based aggregation module weights (i.e., $\boldsymbol{\Phi}_{TA}$) as well as the same neural network architecture (i.e., $f_U(\cdot; \mathcal{W}_U, D_U)$). As a result, the proposed MHGphormer is adaptable to any arbitrary number of users. When the proposed MHGphormer is trained, it can be applied to systems with different number of users. This is different from conventional fully connected networks, which require their parameters to be scaled according to the number of users and re-training for different scenarios.

E. Loss Function Design and Training

The mapping function $\mathcal{F}(\cdot)$ is characterized by the network parameters. We denote the set of all neural network parameters by $\boldsymbol{\Phi} = \{\boldsymbol{\Phi}_{FP}, \boldsymbol{\Phi}_{TA}, \boldsymbol{\Phi}_{DNN}\}$. We reformulate problem (14) as follows:

$$\begin{aligned}\underset{\boldsymbol{\Phi}}{\text{maximize}}\quad & \mathbb{E}\left\{\sum_{u\in\mathcal{U}}\sum_{s\in\mathcal{S}} r_{u,s} - \zeta\sum_{u\in\mathcal{U}}\left(r_{u,\min} - \sum_{s\in\mathcal{S}} r_{u,s}\right)\right\}\\ \text{subject to}\quad & \{\mathbf{P}, \mathbf{b}, \boldsymbol{\Theta}\} = \mathcal{F}\left(\mathbf{X}; \boldsymbol{\Phi}\right),\end{aligned} \tag{30}$$

where the expectation is with respect to the distances between network entities (i.e., BS, RIS, and users). The QoS constraint C5 is added to the objective function in problem (30) as a penalty term with penalizing weight coefficient ζ. To train the proposed MHGphormer based on (30), we adopt mini-batch gradient descent and define the loss function for each training

epoch as follows:

$$\mathscr{L}_k(\mathbf{P},\mathbf{b},\mathbf{\Theta};\mathbf{\Phi}) = \frac{1}{B}\sum_{i=1}^{B}\Bigg(-\sum_{u\in\mathcal{U}}\sum_{s\in\mathcal{S}} r_{u,s}(i) + \zeta_k \sum_{u\in\mathcal{U}} \text{ReLU}\Big(r_{u,\min} - \sum_{s\in\mathcal{S}} r_{u,s}(i)\Big)\Bigg), \quad k=1,\ldots,K, \tag{31}$$

where $\mathscr{L}_k(\cdot)$ is the loss function of the k-th training epoch, B and K denote the size of the mini-batch and the number of training epochs, respectively, and $r_{u,s}(i)$ is the obtained data rate of user $u \in \mathcal{U}$ using sub-band $s \in \mathcal{S}$ for the i-th mini-batch sample. For QoS constraint C5 during the learning procedure, if the constraint is not satisfied for user u, i.e., $\big(r_{u,\min} - \sum_{s\in\mathcal{S}} r_{u,s}\big) > 0$, then the penalty term enforces network parameters $\mathbf{\Phi}$ to be updated in a way to satisfy the constraint. On the other hand, if $\big(r_{u,\min} - \sum_{s\in\mathcal{S}} r_{u,s}\big) \leq 0$, the penalty term does not have an impact on the loss function. Moreover, the penalizing weight coefficient $\zeta_k \geq 0$ in each training epoch is updated as follows:

$$\zeta_{k+1} = \text{ReLU}\left(\zeta_k + \frac{1}{B}\sum_{i=1}^{B}\sum_{u\in\mathcal{U}}\Big(r_{u,\min} - \sum_{s\in\mathcal{S}} r_{u,s}(i)\Big)\right). \tag{32}$$

The proposed MHGphormer is trained to minimize the loss function (31) using Adam optimizer [45] in an unsupervised manner[3]. To construct the training dataset, we generate samples of users' locations in order to obtain the distance information and the channel model in (6). We uniformly sample the training data from the training dataset. In the testing phase, given the testing data, i.e., the locations and the users' minimum data rate as input, the trained network with parameters $\mathbf{\Phi}$ is used to obtain the precoding matrices, RIS phase shifts, and sub-band bandwidth allocation without channel estimation. The proposed MHGphormer learning algorithm is summarized in Algorithm 1. Note that the channel model in (6) is only for generating training samples. Once the network has been trained at the BS, the geographical location information as well as the users' minimum data rate are fed to the network to obtain the system parameters. Additionally, the type-specific DNNs as well as both real and complex weights in the network parameters $\mathbf{\Phi}$ are trained simultaneously through backpropagation to minimize the loss function in (31).

Algorithm 1 Proposed MHGphormer Learning Algorithm

1: **Input**: Heterogeneous graph $\mathcal{G}(\mathcal{V},\mathcal{E},\Psi)$, set of feature matrices $\mathcal{X} := \{\mathbf{X}_{\psi_U},\mathbf{X}_{\psi_B},\mathbf{X}_{\psi_R}\}$, metapaths sets $\{\mathcal{P}_U,\mathcal{P}_B,\mathcal{P}_R\}$, initialize network parameters $\mathbf{\Phi}$, mini-batch size B, number of training epochs K, initialize penalizing weight coefficient ζ_0.
2: Use MNFA module to obtain the aggregated feature information vectors $\Big(\mathbf{x}^{agg}_{1,\psi_U},\ldots,\mathbf{x}^{agg}_{U,\psi_U},\mathbf{x}^{agg}_{B,\psi_B},\mathbf{x}^{agg}_{R,\psi_R}\Big)$.
3: *Unsupervised Training*:
4: Set training epoch counter $k \leftarrow 0$.
5: **while** $k \leq K$
6: Project the input features into the same latent space using (21) and (22) and obtain $\big(\mathbf{x}^{FP}_{1,\psi_U},\ldots,\mathbf{x}^{FP}_{U,\psi_U},,\mathbf{x}^{FP}_{B,\psi_B},\mathbf{x}^{FP}_{R,\psi_R}\big)$.
7: Capture and combine the mutual information of the node types and metapaths by performing transformer-based aggregation using (23) to calculate the embedding values $\big(\mathbf{x}^{TA}_{1,\psi_U},\ldots,\mathbf{x}^{TA}_{U,\psi_U},\mathbf{x}^{TA}_{B,\psi_B},\mathbf{x}^{TA}_{R,\psi_R}\big)$.
8: Calculate the loss function (31) by passing the embedding values of each node type to the designed DNNs $f_U(\cdot)$, $f_B(\cdot)$ and $f_R(\cdot)$.
9: Update $\mathbf{\Phi}$ to minimize the obtained loss function $\mathscr{L}_k(\cdot)$ using Adam optimizer [45].
10: Update penalizing weight coefficient ζ_k using (32).
11: $k \leftarrow k+1$
12: **end while**
13: **Training Output** Trained network with parameters $\mathbf{\Phi}$
14: *Testing Phase*:
15: Use the trained network $\mathcal{F}(\cdot;\mathbf{\Phi})$ to solve problem (14) based on input testing data.
16: **Testing Output** System parameters $\{\mathbf{P},\mathbf{b},\mathbf{\Theta}\}$.

F. Computational Complexity

We now present the computational complexity of our proposed MHGphormer. For the MNFA module in the pre-training step, the computational complexity is $\mathcal{O}(U)$ based on the pre-defined metapaths in (18) for all node types. The computational complexity of this step can be considered as a constant when we determine the computational complexity of the algorithm in the training phase. In the training phase, the users share the same parameters. As a result, in the feature projection step, the computation complexity for all node types is $\mathcal{O}(Z_{FP})$. For the transformer-based aggregation module, the computational complexity is similar for all the nodes and is denoted as $\mathcal{O}(Z_{FP}Z_{TA}+Z_{FP}^2)$. In the final step, we consider that the dimension of hidden units for each neural network is similar to its output dimension. As a result, the computational complexity of feed-forward networks for the user, RIS, and BS node types are $\mathcal{O}(Z_{FP}SN_{\text{t}}N_{\text{r}} + D_pS^2N_{\text{t}}^2N_{\text{r}}^2)$, $\mathcal{O}(Z_{FP}L + D_rL^2)$, and $\mathcal{O}(Z_{FP}S + D_bS^2)$, respectively. Finally, after discarding the lower order terms, the overall computational complexity of the training phase is as follows:

$$\mathcal{O}(Z_{TA}Z_{FP} + Z_{FP}^2 + Z_{FP}SN_{\text{t}}N_{\text{r}} + D_pS^2N_{\text{t}}^2N_{\text{r}}^2 + Z_{FP}L + D_rL^2 + Z_{FP}S + D_bS^2), \tag{33}$$

which shows that the computational complexity is independent of the number of users U.

IV. Performance Evaluation

In this section, we evaluate the performance of our proposed MHGphormer learning algorithm and compare it with three baseline schemes. The code is available at https://github.com/Ali-Meh619/MHGphormer.

A. Experimental Setup

We simulate a RIS-aided MU-MIMO THz system where the (x,y,z)-coordinates of the BS and the RIS locations in meters are $(25,-20,-5)$ and $(0,0,0)$, respectively. The UPA of the BS and UPA for the RIS are placed on the (x,z)-plane and (y,z)-plane, respectively. Six users are randomly and uniformly distributed within a rectangular area $[0,15]\times$

[3]In this paper, we consider sum-rate maximization objective function. However, other utility functions, such as max-min rate and energy efficiency, can be adopted as the loss function of the proposed MHGphormer.

TABLE I: List of Simulation Parameters

Parameters	Value
THz spectrum range $f_{\text{start}} - f_{\text{end}}$	$0.380 - 0.4$ THz
Number of sub-bands S	5
Guard band bandwidth b_{g}	0.75 GHz [7]
Sub-band maximum bandwidth $b_{\max}$	4 GHz [8]
BS maximum power $P_{\max}$	30 dBm
Noise spectral density N_0	-174 dBm/Hz [20]
Number of antennas at the BS N_{t}, N_x, N_y	32, 16, 2
Number of antennas at the user device N_{r}	2
Number of reflecting elements at RIS L, L_x, L_y	64, 8, 8
Antenna element spacing ϵ_{user}, ϵ_{BS}, ϵ_{RIS}	395 μm
Antenna gain G_u, G_{BS}	15, 25 dBi
User minimum data rate $r_{u,\min}$	12.5 Gbps

$[0, 25]$ in the (x, y)-plane with $z = -10$. The ULA for each user is configured parallel to the x-axis. As illustrated in Fig. 2(b), we consider the absorption coefficient values based on HITRAN database [34] for the standard atmosphere with a water vapor density of 1.5 g/m^3 and $15°C$ temperature.

Unless specified otherwise, based on the system setting and simulation parameters in Table I, we generate 15,000 samples, where 12,000 samples are used for training, and the remaining 3,000 samples are used for testing. To implement the neural networks, we use PyTorch library [43] and Adam optimizer [45]. The initial learning rate is set to 5×10^{-4}. The constant dimensions Z_{FP} and Z_{TA} are set to 1024 and 256, respectively. We consider the fully connected networks in the final step with two layers, and the hidden dimension unit is similar to the output dimension for each network. The mini-batch size B and the number of training epochs K are set to 256 and 250, respectively. The initial penalizing weight coefficient ζ_0 is equal to 12×10^9.

We conduct simulations using a computing server with an Intel Silver 4216 Cascade Lake @ 2.1GHz CPU and four Nvidia Tesla V100 Volta GPUs with 128 GB memory. We compare the performance of our proposed MHGphormer with the following baselines:

- **Homogeneous GNN learning algorithm**: We extend the proposed GNN algorithm in [14] for the RIS-aided MU-MIMO THz system. In the proposed system, the pilot signals and the locations of users are used to jointly optimize the phase shifts and precoding matrices in problem (14).
- **Unsupervised DNN learning algorithm**: We extend the learning algorithm in [20] for the MU-MIMO THz system and include a RIS. The distances between users, BS, and RIS are used as input to the DNN to optimize the precoding, phase shifts, and ASB allocation in problem (14).
- **AO Algorithm**: We extend the AO algorithm in [26] for the RIS-aided MU-MIMO THz system. The users' precoding matrices are obtained by dual decomposition method with block coordinate maximization, while the phase shifts at the RIS are computed sequentially and are obtained in a closed-form expression. For ASB allocation, we use the obtained values in our proposed MHGphormer as the bandwidth of the sub-bands.

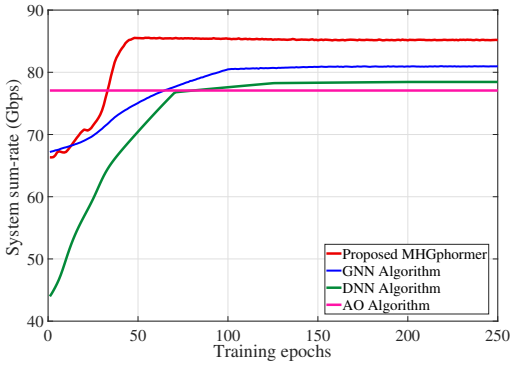

(a)

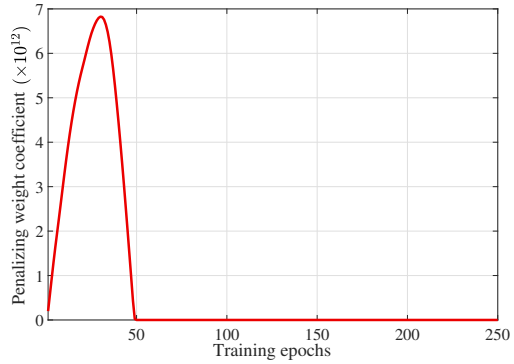

(b)

Fig. 7: (a) Convergence of the proposed MHGphormer learning algorithm and the baseline schemes. (b) Convergence of the penalizing weight coefficient ζ_k for QoS constraint C5.

B. Convergence of the MHGphormer Learning Algorithm

We first investigate the convergence of our proposed MHGphormer. We show the system sum-rate of the MHGphormer and the baselines versus the number of training epochs in Fig. 7(a). Results show that our proposed MHGphormer learning algorithm provides a system sum-rate that is 5.15%, 8.33%, and 8.82% higher than that of GNN learning algorithm, DNN learning algorithm, and AO algorithm, respectively. Moreover, our proposed MHGphormer has a faster convergence compared to the learning-based baselines. Fig. 7(b) shows that the penalizing weight coefficient ζ_k in (32) converges to zero after 50 iterations, which implies that the QoS constraint C5 is satisfied. At the beginning of the training phase, the QoS constraint C5 is not satisfied for the users, i.e., $\left(r_{u,\min} - \sum_{s\in\mathcal{S}} r_{u,s}\right) > 0$. As a result, the penalizing weight coefficient increases based on the update equation (32). Once the constraint is satisfied for the users, i.e., $\left(r_{u,\min} - \sum_{s\in\mathcal{S}} r_{u,s}\right) \leq 0$, the penalizing weight coefficient decreases until it converges to zero.

C. Impact of Number of BS Antennas and RIS Elements

To examine the impact of MIMO signal transmission, we plot the system sum-rate versus the number of antennas at the BS, N_{t}, in Fig. 8. The number of elements in the vertical direction is fixed (i.e., $N_y = 2$) and we vary the number of elements in the horizontal direction (i.e., N_x). We observe that increasing N_{t} improves the sum-rate for all the

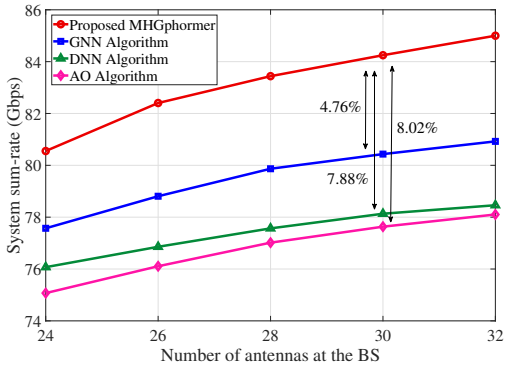

Fig. 8: System sum-rate versus the number of antennas N_{t} at the BS.

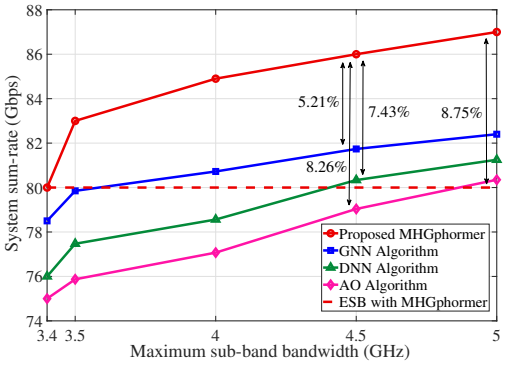

Fig. 10: System sum-rate versus the maximum sub-band bandwidth $b_{\max}$.

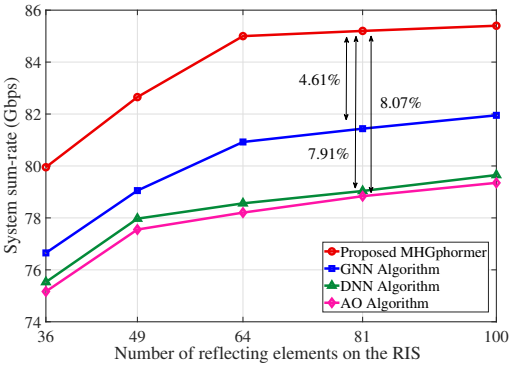

Fig. 9: System sum-rate versus the number of reflecting elements L on the RIS.

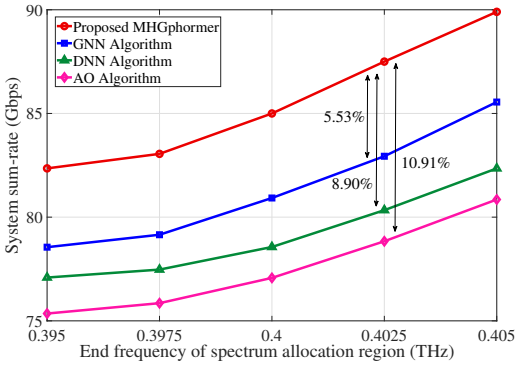

Fig. 11: System sum-rate versus the end frequency of spectrum allocation region f_{end}.

considered algorithms. This indicates that optimal precoding design can provide users with high data rates in THz systems. Moreover, Fig. 8 shows that the performance improvement of the RIS-aided MU-MIMO THz system with the proposed MHGphormer over the baseline schemes increases with the value of N_{t}. In particular, when N_{t} is equal to 30 (i.e., $N_y = 2$, $N_x = 15$), the proposed MHGphormer achieves a system sum-rate that is 4.76%, 7.88%, and 8.02% higher than that of homogeneous GNN, unsupervised DNN, and AO algorithms, respectively.

In Fig. 9, we vary the number of reflecting elements L in the RIS and investigate the system sum-rate. We vary the number of elements in both vertical and horizontal dimensions while they are equal (i.e., $L_x = L_y$). We observe that having a RIS in the system can improve the system sum-rate for all the algorithms. This is because the RIS creates an additional propagation channel which improves the coverage area. In addition, more reflecting elements in the RIS brings a higher flexibility for controlling the phase shifts. Moreover, the performance of the proposed MHGphormer improves with the value of L compared to the baseline schemes. In particular, when L is equal to 81 (i.e., $L_x = L_y = 9$), the proposed MHGphormer achieves a system sum-rate that is 4.61%, 7.91%, and 8.07% higher than that of GNN, DNN, and AO baseline schemes, respectively.

D. Impact of ASB Allocation and Molecular Absorption Coefficient

To study the impact of ASB allocation, we compare the system sum-rate by varying the maximum sub-band bandwidth $b_{\max}$. We also consider ESB allocation with MHGphormer, in which sub-bands have equal bandwidth (i.e., 3.4 GHz) and the precoding matrices and phase shifts are optimized by our proposed MHGphormer. In Fig. 10, by increasing $b_{\max}$, the system sum-rate for all the algorithms is improved compared to ESB allocation. The reason for this is that larger $b_{\max}$ offers more flexibility for ASB allocation. Our proposed MHGphormer achieves 8.75% higher system sum-rate compared to the ESB allocation with MHGphormer when $b_{\max}$ is equal to 5 GHz. Additionally, by increasing $b_{\max}$, our proposed MHGphormer learning algorithm shows better performance compared to the baseline schemes in terms of system sum-rate. In particular, the RIS-aided MU-MIMO system with the proposed MHGphormer achieves a system sum-rate that is 5.21%, 7.43%, and 8.26% higher than that of GNN, DNN, and AO algorithms, respectively.

To investigate the impact of the molecular absorption coefficient on the RIS-aided MU-MIMO THz systems, we vary f_{end} as the end point of the THz TW spectrum. In Fig. 11, we observe that all the algorithms exhibit an improvement in the system sum-rate as the f_{end} increases. At first, this is

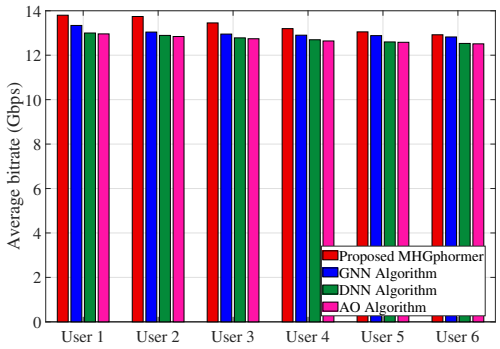

Fig. 12: Average achievable bitrate for each user.

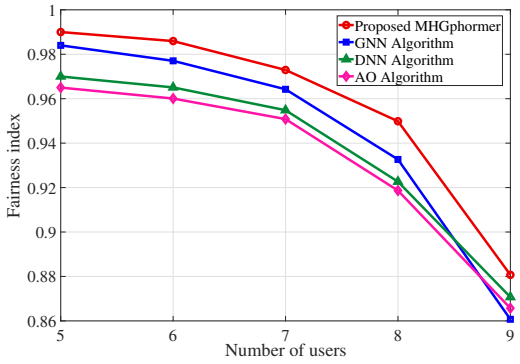

Fig. 13: Jain fairness index versus the number of users U.

due to an increase in the allocated bandwidth to each sub-band. As shown in Fig. 2(b), the molecular absorption loss $k_{\text{abs}}(f)$ decreases by increasing f_{end} in the $0.395 - 0.405$ THz spectrum range. When compared to other baselines, our proposed MHGphormer shows the system sum-rate performance improvement. When f_{end} is equal to 0.4025 THz, the RIS-aided MU-MIMO system with MHGphormer achieves a system sum-rate that is 5.53%, 8.90%, and 10.91% higher than that of GNN, DNN, and AO algorithms, respectively.

E. Investigating User Average Bitrate and Fairness Behaviour

In Fig. 12, we plot the average bitrate for each user in descending order. That is, the user with the highest average bitrate is referred to as user 1, while the user with the lowest average bitrate is referred to as user 6. Considering the QoS constraint C5 in problem (14), results show that the users achieve higher bitrates in an RIS-aided MU-MIMO THz system with the proposed MHGphormer learning algorithm compared to GNN and DNN learning algorithms as well as AO algorithm. This is because we model the network topology as a heterogeneous graph in a fine-grained manner and consider the transmission links as edges and the information of all entities (i.e., BS, RIS, and users) as different types of nodes. Aggregation of feature information of different node types in our proposed MHGphormer leads to QoS improvement.

To investigate the fairness behaviour for the MHGphormer, we vary the number of users and plot the fairness index in Fig. 13. The Jain fairness index is defined as $\frac{\left(\sum_{u\in\mathcal{U}}\sum_{s\in\mathcal{S}} r_{u,s}\right)^2}{U\sum_{u\in\mathcal{U}}\sum_{s\in\mathcal{S}} r_{u,s}^2}$, which shows how fair the resources are allocated to the users in terms of bitrate. Moreover, our MHGphormer is scalable with respect to the number of users once it has been trained. To investigate the fairness behaviour, we train the MHGphormer and GNN learning algorithms with 6 users. The training of DNN and the execution of the AO algorithm are conducted separately for different number of users. Results show that the fairness index decreases for all the algorithms in the RIS-aided MU-MIMO THz system when we increase the number of users. This is because an increase in the number of QoS constraints in problem (14) results in a smaller feasible set. Moreover, our proposed MHGphormer has better fairness behaviour compared to homogeneous GNN learning algorithm, as well as DNN and AO algorithms, which require re-training for scenarios with different number of users.

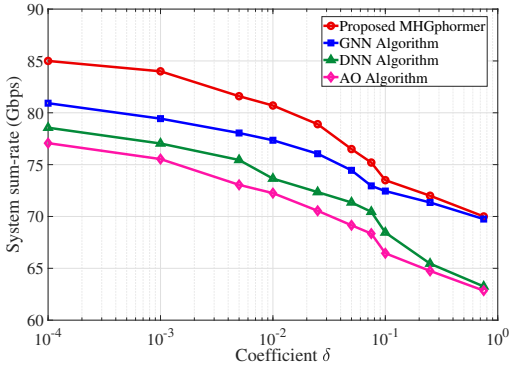

Fig. 14: System sum-rate for imperfect user location estimation.

F. Impact of Imperfect User Location Estimation

Finally, we investigate the robustness of the proposed MHGphormer to imperfect user location estimation based on the statistical location estimation error in [46]. We denote $\hat{\mathbf{g}}_u = \mathbf{g}_u + \Delta\mathbf{g}_u$ as the estimated location of user $u \in \mathcal{U}$, where $\Delta\mathbf{g}_u$ is the location estimation error. We consider that the elements in vector $\Delta\mathbf{g}_u$ follow Gaussian distribution with zero mean and variance $\delta \|\mathbf{g}_u\|_2^2$, where the coefficient $\delta \in [0, 1)$ measures the significance of the error. In Fig. 14, we evaluate the achievable system sum-rate under imperfect user location estimation for all the algorithms. We observe the performance degradations in all considered algorithms due to imperfect user location estimation. In particular, when δ is equal to 0.1, the proposed MHGphormer can retain 84.35% of the system sum-rate that can be achieved with perfect user location estimation.

V. Conclusion

In this paper, we investigated the sum-rate maximization problem for RIS-aided MU-MIMO THz systems. We studied the joint optimization of precoding, phase shifts, and ASB allocation. Since the THz sub-band bandwidth is not known beforehand in ASB allocation, accurate channel estimation is challenging. To overcome this issue, we proposed an unsupervised MHGphormer learning algorithm to solve the problem by bypassing the channel estimation phase. The

proposed MHGphormer directly maps the location information and users' minimum data rate as input to the optimized system parameters. The MHGphormer has the permutation invariance/equivariance property and can be applied to networks with different number of users. Through simulations, we showed that our proposed MHGphormer learning algorithm has a faster convergence compared to the learning-based algorithms. For a RIS-aided MU-MIMO THz system with six users, the proposed MHGphormer achieves a system sum-rate that is 5.15%, 8.33%, and 8.82% higher than that of homogeneous GNN, unsupervised DNN, and AO algorithms, respectively. We also demonstrated the system sum-rate improvements obtained from using RIS, MIMO, and ASB in multiuser THz systems. For future work, we plan to study the impact of optimizing the number of sub-bands in multiple THz TWs.

APPENDIX

Definition [47]: A transformation $\mathcal{T}_\pi : \mathbb{R}^{d\times N} \to \mathbb{R}^{d\times N}$ is a permutation if $\mathcal{T}_\pi(\mathbf{X}) = \mathbf{X}\mathbf{P}_\pi$, where matrix $\mathbf{X} \in \mathbb{R}^{d\times N}$ is the input, $\mathbf{P}_\pi \in \{\{0,1\}^{N\times N} |\ \mathbf{P}_\pi^T\mathbf{1}_N = \mathbf{1}_N^T\mathbf{P}_\pi = \mathbf{I}_N\}$ is the permutation matrix, and $\mathbf{1}_N$ denotes an all-ones vector.

Definition [48]: An operator $O_e : \mathbb{R}^{d\times N} \to \mathbb{R}^{d\times N}$ is said to be permutation equivariant if $\mathcal{T}_\pi(O_e(\mathbf{X})) = O_e(\mathcal{T}_\pi(\mathbf{X}))$ for any permutation matrix $\mathbf{P}_\pi$. Moreover, an operator $O_i : \mathbb{R}^{d\times N} \to \mathbb{R}^{d\times N}$ is permutation invariant if $\mathcal{T}_\pi(O_i(\mathbf{X})) = O_i(\mathbf{X})$ for any permutation matrix $\mathbf{P}_\pi$.

Proposition 1: *MHGphormer with the proposed self-attention mechanism in (23) is permutation equivariant.*

Proof: In (23), the self-attention operator can be written as follows:

$$\begin{aligned}
&O_e(\mathcal{T}_\pi(\mathbf{X}))\\
&= \beta\mathbf{W}_V\mathcal{T}_\pi(\mathbf{X})\ \text{softmax}\Big(\left(\mathbf{W}_K\mathcal{T}_\pi(\mathbf{X})\right)^T\mathbf{W}_Q\mathcal{T}_\pi(\mathbf{X})\Big)\\
&\quad + \mathcal{T}_\pi(\mathbf{X})\\
&= \beta\mathbf{W}_V\mathbf{X}\mathbf{P}_\pi\text{softmax}\Big(\left(\mathbf{W}_K\mathbf{X}\mathbf{P}_\pi\right)^T\mathbf{W}_Q\mathbf{X}\mathbf{P}_\pi\Big)\\
&\quad + \mathbf{X}\mathbf{P}_\pi\\
&= \beta\mathbf{W}_V\mathbf{X}\mathbf{P}_\pi\text{softmax}\Big(\mathbf{P}_\pi^T\left(\mathbf{W}_K\mathbf{X}\right)^T\mathbf{W}_Q\mathbf{X}\mathbf{P}_\pi\Big)\\
&\quad + \mathbf{X}\mathbf{P}_\pi\\
&= \beta\mathbf{W}_V\mathbf{X}\underbrace{\mathbf{P}_\pi\mathbf{P}_\pi^T}_{\mathbf{I}_N}\text{softmax}\Big(\left(\mathbf{W}_K\mathbf{X}\right)^T\mathbf{W}_Q\mathbf{X}\Big)\mathbf{P}_\pi\\
&\quad + \mathbf{X}\mathbf{P}_\pi\\
&= \Big(\beta\mathbf{W}_V\mathbf{X}\text{softmax}\Big(\left(\mathbf{W}_K\mathbf{X}\right)^T\mathbf{W}_Q\mathbf{X}\Big) + \mathbf{X}\Big)\mathbf{P}_\pi\\
&= \mathcal{T}_\pi(O_e(\mathbf{X})).
\end{aligned}$$

Note that $\mathbf{P}_\pi\mathbf{P}_\pi^T = \mathbf{I}_N$ since $\mathbf{P}_\pi$ is an orthogonal matrix. Also, it can be shown that:

$$\text{softmax}\Big(\mathbf{P}_\pi^T\mathbf{X}\mathbf{P}_\pi\Big) = \mathbf{P}_\pi^T\text{softmax}(\mathbf{X})\mathbf{P}_\pi.$$

The softmax function is applied to the matrix input column-wise, similar to the definition in (16).

Proposition 2: *MHGphormer, which includes a self-attention mechanism with learnable query matrix, is permutation invariant.*

Proof: The self-attention operator with learnable query matrix can be expressed as follows:

$$\begin{aligned}
&O_i(\mathcal{T}_\pi(\mathbf{X}))\\
&= \mathbf{W}_V\mathcal{T}_\pi(\mathbf{X})\text{softmax}\Big(\left(\mathbf{W}_K\mathcal{T}_\pi(\mathbf{X})\right)^T\mathbf{W}_Q\Big)\\
&= \mathbf{W}_V\mathbf{X}\mathbf{P}_\pi\text{softmax}\Big(\left(\mathbf{W}_K\mathbf{X}\mathbf{P}_\pi\right)^T\mathbf{W}_Q\Big)\\
&= \mathbf{W}_V\mathbf{X}\mathbf{P}_\pi\text{softmax}\Big(\mathbf{P}_\pi^T\left(\mathbf{W}_K\mathbf{X}\right)^T\mathbf{W}_Q\Big)\\
&= \mathbf{W}_V\mathbf{X}\underbrace{\mathbf{P}_\pi\mathbf{P}_\pi^T}_{\mathbf{I}_N}\text{softmax}\Big(\left(\mathbf{W}_K\mathbf{X}\right)^T\mathbf{W}_Q\Big)\\
&= \mathbf{W}_V\mathbf{X}\text{softmax}\Big(\left(\mathbf{W}_K\mathbf{X}\right)^T\mathbf{W}_Q\Big)\\
&= O_i(\mathbf{X}).
\end{aligned}$$

REFERENCES

[1] A. Mehrabian and V. W.S. Wong, "Adaptive bandwidth allocation in multiuser MIMO THz systems with graph-transformer networks," accepted for publication in *Proc. of IEEE Int. Conf. Commun. (ICC)*, Denver, CO, Jun. 2024.

[2] C.-X. Wang, J. Wang, S. Hu, Z. H. Jiang, J. Tao, and F. Yan, "Key technologies in 6G terahertz wireless communication systems: A survey," *IEEE Veh. Technol. Mag.*, vol. 16, no. 4, pp. 27–37, Dec. 2021.

[3] Z. Wan, Z. Gao, F. Gao, M. Di Renzo, and M.-S. Alouini, "Terahertz massive MIMO with holographic reconfigurable intelligent surfaces," *IEEE Trans. Commun.*, vol. 69, no. 7, pp. 4732–4750, Jul. 2021.

[4] H. Yuan, N. Yang, X. Ding, C. Han, K. Yang, and J. An, "Cluster-based multi-carrier hybrid beamforming for massive device terahertz communications," *IEEE Trans. Commun.*, vol. 70, no. 5, pp. 3407–3420, May 2022.

[5] C. Han, A. O. Bicen, and I. F. Akyildiz, "Multi-wideband waveform design for distance-adaptive wireless communications in the terahertz band," *IEEE Trans. Signal Process.*, vol. 64, no. 4, pp. 910–922, Feb. 2016.

[6] H. Zhang, Y. Duan, K. Long, and V. C. M. Leung, "Energy efficient resource allocation in terahertz downlink NOMA systems," *IEEE Trans. Commun.*, vol. 69, no. 2, pp. 1375–1384, Feb. 2021.

[7] A. Shafie, N. Yang, S. A. Alvi, C. Han, S. Durrani, and J. M. Jornet, "Spectrum allocation with adaptive sub-band bandwidth for terahertz communication systems," *IEEE Trans. Commun.*, vol. 70, no. 2, pp. 1407–1422, Feb. 2021.

[8] A. Shafie, N. Yang, C. Han, and J. M. Jornet, "Novel spectrum allocation among multiple transmission windows for terahertz communication systems," *IEEE Trans. Veh. Technol.*, vol. 71, no. 12, pp. 13 415–13 421, Dec. 2022.

[9] H. Sarieddeen, M.-S. Alouini, and T. Y. Al-Naffouri, "An overview of signal processing techniques for terahertz communications," *Proc. of the IEEE*, vol. 109, no. 10, pp. 1628–1665, Oct. 2021.

[10] C. Huang, Z. Yang, G. C. Alexandropoulos, K. Xiong, L. Wei, C. Yuen, Z. Zhang, and M. Debbah, "Multi-hop RIS-empowered terahertz communications: A DRL-based hybrid beamforming design," *IEEE J. Sel. Areas Commun.*, vol. 39, no. 6, pp. 1663–1677, Jun. 2021.

[11] X. Zhao, K. Xu, S. Ma, S. Gong, G. Yang, and C. Xing, "Joint transceiver optimization for IRS-aided MIMO communications," *IEEE Trans. Commun.*, vol. 70, no. 5, pp. 3467–3482, May 2022.

[12] B. Zheng, C. You, and R. Zhang, "Double-IRS assisted multi-user MIMO: Cooperative passive beamforming design," *IEEE Trans. Wireless Commun.*, vol. 20, no. 7, pp. 4513–4526, Jul. 2021.

[13] K. Zhi, C. Pan, H. Ren, K. Wang, M. Elkashlan, M. D. Renzo, R. Schober, H. V. Poor, J. Wang, and L. Hanzo, "Two-timescale design for reconfigurable intelligent surface-aided massive MIMO systems with imperfect CSI," *IEEE Trans. Inf. Theory*, vol. 69, no. 5, pp. 3001–3033, May 2023.

[14] T. Jiang, H. V. Cheng, and W. Yu, "Learning to reflect and to beamform for intelligent reflecting surface with implicit channel estimation," *IEEE J. Sel. Areas Commun.*, vol. 39, no. 7, pp. 1931–1945, Jul. 2021.

[15] Z. Zhang, T. Jiang, and W. Yu, "Learning based user scheduling in reconfigurable intelligent surface assisted multiuser downlink," *IEEE J. Sel. Topics Signal Process.*, vol. 16, no. 5, pp. 1026–1039, Aug. 2022.
[16] V. Schram, A. Moldovan, and W. H. Gerstacker, "Compressive sensing for indoor THz channel estimation," in *Proc. of Asilomar Conf. on Sig., Syst., and Comput.*, Pacific Grove, CA, Oct. 2018.
[17] W. Cui, K. Shen, and W. Yu, "Spatial deep learning for wireless scheduling," *IEEE J. Sel. Areas Commun.*, vol. 37, no. 6, pp. 1248–1261, Jun. 2019.
[18] C. Huang, G. C. Alexandropoulos, C. Yuen, and M. Debbah, "Indoor signal focusing with deep learning designed reconfigurable intelligent surfaces," in *Proc. IEEE Int. Workshop Signal Process. Adv. Wireless Commun. (SPAWC)*, Cannes, France, Jul. 2019.
[19] R. Liu, M. Lee, G. Yu, and G. Y. Li, "User association for millimeter-wave networks: A machine learning approach," *IEEE Trans. Commun.*, vol. 68, no. 7, pp. 4162–4174, Jul. 2020.
[20] A. Shafie, C. Lit, N. Yang, X. Zhou, and T. Q. Duong, "An unsupervised learning approach for spectrum allocation in terahertz communication systems," in *Proc. of IEEE Global Commun. Conf. (GLOBECOM)*, Rio de Janeiro, Brazil, Dec. 2022.
[21] Z. Hu, Y. Dong, K. Wang, and Y. Sun, "Heterogeneous graph transformer," in *Proc. Int'l World Wide Web Conf. (WWW)*, Taipei, Taiwan, Apr. 2020.
[22] J. Kim, H. Lee, S.-E. Hong, and S.-H. Park, "A bipartite graph neural network approach for scalable beamforming optimization," *IEEE Trans. Wireless Commun.*, vol. 22, no. 1, pp. 333–347, Jan. 2023.
[23] J. Guo and C. Yang, "Learning power allocation for multi-cell-multi-user systems with heterogeneous graph neural networks," *IEEE Trans. on Wireless Commun.*, vol. 21, no. 2, pp. 884–897, Feb. 2022.
[24] X. Wang, H. Ji, C. Shi, B. Wang, Y. Ye, P. Cui, and P. S. Yu, "Heterogeneous graph attention network," in *Proc. Int'l World Wide Web Conf. (WWW)*, San Francisco, CA, May 2019.
[25] J. Chen, K. Gao, G. Li, and K. He, "NAGphormer: A tokenized graph transformer for node classification in large graphs," in *Proc. Int'l Conf. Learn. Representations (ICLR)*, Kigali, Rwanda, May 2023.
[26] N. S. Perović, L.-N. Tran, M. D. Renzo, and M. F. Flanagan, "On the maximum achievable sum-rate of the RIS-aided MIMO broadcast channel," *IEEE Trans. Signal Process.*, vol. 70, pp. 6316–6331, 2022.
[27] K. Dovelos, M. Matthaiou, H. Q. Ngo, and B. Bellalta, "Channel estimation and hybrid combining for wideband terahertz massive MIMO systems," *IEEE J. Sel. Areas Commun.*, vol. 39, no. 6, pp. 1604–1620, Jun. 2021.
[28] C. Han, A. O. Bicen, and I. F. Akyildiz, "Multi-ray channel modeling and wideband characterization for wireless communications in the terahertz band," *IEEE Trans. Wireless Commun.*, vol. 14, no. 5, pp. 2402–2412, May 2014.
[29] M. Li, F. Zhang, X. Zhang, Y. Lyu, and W. Fan, "Omni-directional pathloss measurement based on virtual antenna array with directional antennas," *IEEE Trans. Veh. Technol.*, vol. 72, no. 2, pp. 2576 – 2580, Feb. 2022.
[30] Y. Pan, C. Pan, S. Jin, and J. Wang, "RIS-aided near-field localization and channel estimation for the terahertz system," *IEEE J. Sel. Topics Signal Process.*, vol. 17, no. 4, pp. 878–892, Jul. 2023.
[31] W. Yan, W. Hao, C. Huang, G. Sun, O. Muta, H. Gacanin, and C. Yuen, "Beamforming analysis and design for wideband THz reconfigurable intelligent surface communications," *IEEE J. Sel. Areas Commun.*, vol. 41, no. 8, pp. 2306–2320, Aug. 2023.
[32] R. Su, L. Dai, and D. W. K. Ng, "Wideband precoding for RIS-aided THz communications," *IEEE Trans. Commun.*, vol. 71, no. 6, pp. 3592–3604, Jun. 2023.
[33] J. M. Jornet and I. F. Akyildiz, "Channel modeling and capacity analysis for electromagnetic wireless nanonetworks in the terahertz band," *IEEE Trans. Wireless Commun.*, vol. 10, no. 10, pp. 3211–3221, Oct. 2011.
[34] E. A. L. S. Rothman, "The HITRAN 2008 molecular spectroscopic database," *J. Quant. Spectrosc. Radiat. Transf.*, vol. 110, no. 9-10, pp. 533–572, Jun. 2009.
[35] K. Hornik, M. Stinchcombe, and H. White, "Multilayer feedforward networks are universal approximators," *Neural Netw.*, vol. 2, no. 5, pp. 359–366, Jan. 1989.
[36] A. Mehrabian, S. Bahrami, and V. W.S. Wong, "A dynamic Bernstein graph recurrent network for wireless cellular traffic prediction," in *Proc. of IEEE Int. Conf. Commun. (ICC)*, Rome, Italy, May 2023.
[37] Y. Yu, J. Chen, T. Gao, and M. Yu, "DAG-GNN: DAG structure learning with graph neural networks," in *Proc. Int'l Conf. Machine Learning (ICML)*, Long Beach, CA, Jun. 2019.
[38] H. Kim, H. Chen, M. F. Keskin, Y. Ge, K. Keykhosravi, G. C. Alexandropoulos, S. Kim, and H. Wymeersch, "RIS-enabled and access-point-free simultaneous radio localization and mapping," accepted for publication in *IEEE Trans. Wireless Commun.*, 2023.
[39] X. Yang, M. Yan, S. Pan, X. Ye, and D. Fan, "Simple and efficient heterogeneous graph neural network," in *Proc. of AAAI Conf. on Artif. Intell.*, Washington, DC, Feb. 2023.
[40] X. Fu, J. Zhang, Z. Meng, and I. King, "MAGNN: Metapath aggregated graph neural network for heterogeneous graph embedding," in *Proc. Int'l World Wide Web Conf. (WWW)*, Taipei, Taiwan, Apr. 2020.
[41] S. Yun, M. Jeong, R. Kim, J. Kang, and H. J. Kim, "Graph transformer networks," in *Proc. Advances in Neural Inf. Process. Syst. (NeurIPS)*, Vancouver, Canada, Dec. 2019.
[42] A. Vaswani, N. Shazeer, N. Parmar, J. Uszkoreit, L. Jones, A. N. Gomez, Ł. Kaiser, and I. Polosukhin, "Attention is all you need," in *Proc. Advances in Neural Inf. Process. Syst. (NeurIPS)*, Long Beach, CA, Dec. 2017.
[43] A. Paszke, S. Gross, F. Massa, A. Lerer, J. Bradbury, G. Chanan, T. Killeen, Z. Lin, N. Gimelshein, L. Antiga *et al.*, "PyTorch: An imperative style, high-performance deep learning library," in *Proc. Adv. Neural Inf. Process. Syst. (NeurIPS)*, Vancouver, Canada, Dec. 2019.
[44] Z. Wang, Y. Zhou, Y. Zou, Q. An, Y. Shi, and M. Bennis, "A graph neural network learning approach to optimize RIS-assisted federated learning," *IEEE Trans. Wireless Commun.*, vol. 22, no. 9, pp. 6092–6106, Sept. 2023.
[45] D. P. Kingma and J. Ba, "Adam: A method for stochastic optimization," in *Proc. Int'l Conf. Learn. Representations (ICLR)*, San Diego, CA, May 2015.
[46] A. Elzanaty, A. Guerra, F. Guidi, and M.-S. Alouini, "Reconfigurable intelligent surfaces for localization: Position and orientation error bounds," *IEEE Trans. Signal Process.*, vol. 69, pp. 5386–5402, 2021.
[47] M. Artin, *Algebra,* 2nd Edition. Pearson, 2010.
[48] L. Wu, P. Cui, J. Pei, and L. Zhao, *Graph Neural Networks: Foundations, Frontiers, and Applications*. Springer, 2022.

Ali Mehrabian (S'21) received the B.Sc. degree in Electrical Engineering from the Sharif University of Technology (SUT), Tehran, Iran, in 2021. He received the M.A.Sc. degree in Electrical and Computer Engineering from The University of British Columbia (UBC), Vancouver, Canada, in 2023. His research interests include machine learning, time series analysis and forecasting, and optimization in social networks and communication systems.

Vincent W.S. Wong (S'94, M'00, SM'07, F'16) received the B.Sc. degree from the University of Manitoba, Canada, in 1994, the M.A.Sc. degree from the University of Waterloo, Canada, in 1996, and the Ph.D. degree from The University of British Columbia (UBC), Vancouver, Canada, in 2000. From 2000 to 2001, he worked as a systems engineer at PMC-Sierra Inc. (now Microchip Technology Inc.). He joined the Department of Electrical and Computer Engineering at UBC in 2002 and is currently a Professor. His research areas include protocol design, optimization, and resource management of communication networks, with applications to 5G/6G wireless networks, Internet of things, mobile edge computing, smart grid, and energy systems. Dr. Wong is the Editor-in-Chief of *IEEE Transactions on Wireless Communications*. He has served as an Area Editor of *IEEE Transactions on Communications* and *IEEE Open Journal of the Communications Society*, an Associate Editor of *IEEE Transactions on Mobile Computing* and *IEEE Transactions on Vehicular Technology*, and a Guest Editor of *IEEE Journal on Selected Areas in Communications*, *IEEE Internet of Things Journal*, and *IEEE Wireless Communications*. Dr. Wong is the General Co-chair of *IEEE INFOCOM* 2024. He was a Tutorial Co-Chair of *IEEE GLOBECOM*'18, a Technical Program Co-chair of *IEEE VTC*2020-*Fall* and *IEEE SmartGridComm*'14, and a Symposium Co-chair of *IEEE ICC*'18, *IEEE SmartGridComm* ('13, '17) and *IEEE GLOBECOM*'13. He received the Best Paper Award at the *IEEE ICC* 2022 and *IEEE GLOBECOM* 2020. He is the Chair of the IEEE Vancouver Joint Communications Chapter and has served as the Chair of the IEEE Communications Society Emerging Technical Sub-Committee on Smart Grid Communications. Dr. Wong is an IEEE Vehicular Technology Society Distinguished Lecturer (2023−2025) and was an IEEE Communications Society Distinguished Lecturer (2019−2020).